Andreas Kvas, BSc

Estimation of Short- and Long-term Temporal Variations in Earth's Gravity Field from GRACE Data in a Combined Least Squares Adjustment

MASTER'S THESIS

to achieve the university degree of
Diplom-Ingenieur/in

Masters's degree programme: Geomatics Science

submitted to

Graz University of Technology

Supervisor:
Univ.-Prof. Dr.-Ing. Torsten Mayer-Gürr
Institute of Theoretical Geodesy and Satellite Geodesy

Graz, November 2014

Acknowledgments

First and foremost I would like to thank my supervisor Univ.-Prof. Dr.-Ing. Torsten Mayer-Gürr for suggesting the topic of this thesis and his and patience during my scientific work. His supervision and advice made the past months an invaluable learning experience.

I would also like to thank the staff of the Institute of Theoretical Geodesy and Satellite Geodesy at the TU Graz for their feedback and help.

Finally, I am very grateful to my parents and family who have supported me throughout my studies and made the completion of this thesis possible.

AFFIDAVIT

I declare that I have authored this thesis independently, that I have not used other than the declared sources/resources, and that I have explicitly indicated all material which has been quoted either literally or by content from the sources used. The text document uploaded to TUGRAZonline is identical to the present master‘s thesis dissertation.

Date

Signature

Abstract

The gravity field and its variations in time are important observables for the understanding of the Earth's dynamic system. The twin satellites of the GRACE (Gravity Recovery And Climate Experiment) mission have been designed to measure such temporal variations as well as the long-wavelength part of Earth's gravity field with unprecedented accuracy on a global scale.
Due to the sensitivity of GRACE to this time variable signal, mass redistributions which cause temporal gravity field variations have to be considered in the gravity field recovery process. This is typically done by the application of geophysical models to the satellite data. These models however do not perfectly resemble reality, resulting in residual time variable signal in the measurements which deteriorates derived gravity field solutions. To obtain reliable estimates, an appropriate modeling of the time variable gravity signal is therefore unavoidable. The incorporation of temporal variations into the least squares adjustment process is however accompanied by computational challenges. When modeling daily variations as spherical harmonic coefficients up to degree and order 40 within the adjustment process, an additional 1677 unknowns per day have to be considered. For the whole GRACE observation period starting from 2003 until today, this yields total of approximately 7.2 million unknown parameters. A least squares adjustment of this size is not solvable in a sensible time frame, therefore measures to reduce the problem size have to be taken.
In this thesis an integrated approach for the combined estimation of the static gravity field and temporal variations of different time scales is presented. The developed approach is applied to GRACE-L1B data and the effect of different temporal representations is investigated. The capability of the method will be demonstrated on the basis of three computed GRACE-only gravity field models.

Kurzfassung

Das Schwerefeld der Erde und seine zeitliche Änderung stellen wichtige Beobachtungsgrößen in der Erforschung des dynamischen Systems Erde dar. Die Satelliten der GRACE (Gravity Recovery And Climate Experiment) Mission wurden entwickelt um ebendiese zeitlichen Variationen und den langwelligen Anteil des Erdschwerefeldes erstmals mit global Überdeckung hoch genau zu erfassen.
In der Bestimmung von Erdschwerefeldern müssen diese Variationen berücksichtigt werden. Üblicherweise wird dies durch die Reduktion der Satellitendaten über geophysikalische Modelle durchgeführt. Die Modelle bilden jedoch die Wirklichkeit nicht vollständig ab, was dazu führt, dass Restsignal der zeitlichen Änderung in den Daten verbleibt. Um zuverlässige Schwerefeldlösungen zu erhalten ist die Modellierung dieser zeitlichen Variationen daher unumgänglich.
Die Modellierung der zeitlich Variationen stellt allerdings eine rechentechnische Herausforderung dar. Werden tägliche Schwerevariationen in Kugelfunktionskoeffizienten bis Grad und Ordnung 40 angesetzt, ergeben sich pro Tag 1677 zusätzliche Unbekannte. Für den gesamten Beobachtungszeitraum der GRACE Mission startend in 2003 bedeutet das eine Parameteranzahl von ca. 7.2 Millionen. Ein Ausgleich nach kleinsten Quadraten dieser Größe ist nicht in ansprechendem Zeitrahmen lösbar, was Strategien zur Reduktion der Problemgröße erforderlich macht.
In dieser Arbeit wird eine Methode für den gemeinsamen Ausgleich von Kurz- und Langzeitvariationen sowie dem statischen Anteil des Erdchwerefeldes präsentiert. Der entwickelte Ansatz wird auf GRACE-L1B Daten angewendet und verschiedene Repräsentationen des zeitvariablen Erschwerefeldanteils werden untersucht. Die Leistungsfähigkeit der kombinierten Ausgleichung wird anhand von drei abgeleiteten GRACE-only Lösungen gezeigt.

Contents

1 Introduction

Precise knowledge of Earth's gravity field and its variations in time is crucial for understanding the dynamic system Earth and its geophysical processes. Dedicated satellites are able to measure these signals and provide an invaluable data basis for geophysics and climate research. Within this context, the twin satellites of the GRACE (Gravity Recovery And Climate Experiment) mission are of special interest. The mission configuration and instrumentation are specifically designed to measure gravity field variations as well as the long-wavelength part of the gravity field with unprecedented accuracy on a global scale.
The minimization of temporal aliasing effects poses a great challenge in GRACE processing. Since the orbital characteristics of GRACE allow an unconstrained, global gravity field solution only after a time period of one month, all processes with higher temporal frequency need to be reduced from the satellite data to comply to the Nyquist sampling theorem (Oppenheim et al., 1999). This is typically done by the application of geophysical models to the satellite data. These models however, do not perfectly resemble reality, resulting in residual temporal signal which deteriorates the gravity field solutions. Another approach is the increase of the temporal resolution of the gravity field estimates as performed by Kurtenbach, 2011 to achieve a higher sampling rate. Introducing these daily gravity field solutions as improved dealiasing product, as performed in the computation of the ITG-Grace2010s gravity field solution (Mayer-Gürr et al., 2010b), does however neglect the correlations with the static part resulting in a underestimation of the formal gravity field errors. To take these correlations into account, a combined modeling of temporal variations and static gravity field is necessary.
It is the goal of this thesis to develop an integrated approach for the incorporation of short- and long-term temporal variations into the gravity field recovery process.

The thesis is organized in the following sections: In chapter 2 an overview of the GRACE mission is given. This includes a description of the spacecraft, its orbital characteristics and a discussion of the temporal aliasing problem of the GRACE mission. Chapter 3 deals with the time variable part of Earth's gravity field. Different mathematical representations are discussed and their existing applications are outlined. In chapter 4 the functional and stochastic model for the GRACE observables used in this thesis is described. This includes the observation equations for POD (precise orbit determination) and KBR (K-Band Ranging System) measurements. A general overview of techniques concerning the least squares adjustment can be found in chapter 5. In chapter 6 the developed algorithm is presented. Based on the derived mathematical representation of normal equations containing temporal variations, a detailed description of the algorithmic implementation is given. The algorithm described in the previous section is applied to the GRACE time series in chapter 7. Following an overview of the gravity field recovery process used in this thesis, different solutions are presented and discussed. Chapter 8 contains a summary of the developed method and an outlook on possible further research.

2 The Satellite Mission GRACE

GRACE is a joint project of NASA (National Aeronautics and Space Administration) and DLR (Deutsches Zentrum für Luft und Raumfahrt). Jointly proposed by the UTCSR (University of Texas at Austin, Center for Space Research), the GFZ (German Research Centre for Geosciences) and the JPL (Jet Propulsion Laboratories) in Pasadena, GRACE was selected in 1997 as second mission in NASA's ESSP (Earth System Science Pathfinder) program. Five years later, on March 17, 2002, the satellite pair was brought into orbit from Plesetsk, Russia by a Rockot launcher. A detailed description of the GRACE mission can be found in Tapley et al., 2004. The mission duration was designed to be about five years, at present the predicted lifetime ranges from twelve to fifteen years (Tapley et al., 2014).
The primary science objective of the GRACE mission is to measure Earth's static and time variable gravity field with unprecedented accuracy. To achieve this objective, the twin satellites are equipped with tailored payload consisting of GPS (Global Positioning System) receivers for position and velocity determination as well as star cameras and accelerometers for attitude and surface force measurements. Additionally, the satellites are interconnected by a K-band microwave link which is able to determine the separation distance between the spacecraft and its rate of change with an accuracy of better than 0.1 $\mu m/s$. This ranging system allows for measurements of the SST-ll (low-low satellite-to-satellite tracking) principle. Orbiting the earth, the satellites are subject to very small accelerations as they pass across contours in the gravity field. Because of the along track separation, these apply first to the leading spacecraft and then the other, resulting in distance variations between them. The mission configuration is especially sensitive to the long-wavelength part of the gravity field signal and therefore mass variations caused by for example the continental hydrological cycle, ice mass loss in glacier systems in Greenland or Antarctica or changes in ocean circulation processes.
The secondary objective of GRACE is to provide globally distributed vertical temperature and humidity profiles by means of GPS radio occultation technique.
The satellite's orbit is nearly circular with an eccentricity e of less than $5 \cdot 10^{-4}$. To achieve a homogeneous data coverage over the whole globe, a near-polar orbit with an inclination of about 89° has been chosen. Due to the orbital height of 400 km to 500 km the GRACE satellites are classified as LEO (Low Earth Orbiter).

2.1 Satellite Layout and Sensors

As basis for the GRACE spacecraft served the CHAMP (Challenging Minisatellite Payload) body design. Both satellites are built identically with a length of about 3 m and a launch mass of about 487 kg. Figure 2.1 shows the layout of the most important instruments on board the spacecraft.

K-Band Ranging System The inter-satellite microwave link is the main instrument for gravity field recovery. It is able to determine distance variations between the two spacecraft with an accuracy of less than 1 μm. The instrument is based on dual frequency measurements in the K- and Ka-band (24 GHz and 32 GHz) sent and received by a Horn-antenna mounted at the front of each satellite. Both satellites carry identical ranging systems except for a frequency shift of 500 kHz to avoid crosstalk. The base frequency is established via an USO (Ultra Stable Oscillator)

GPS Receiver Assembly The GPS (GPS Receiver Assembly) serves as primary system for orbit determination and time synchronization on board of the GRACE satellites. Each spacecraft is equipped with three antennas, with the main antenna mounted on the upper side facing in zenith direction. The rear panel features a GPS backup antenna as well

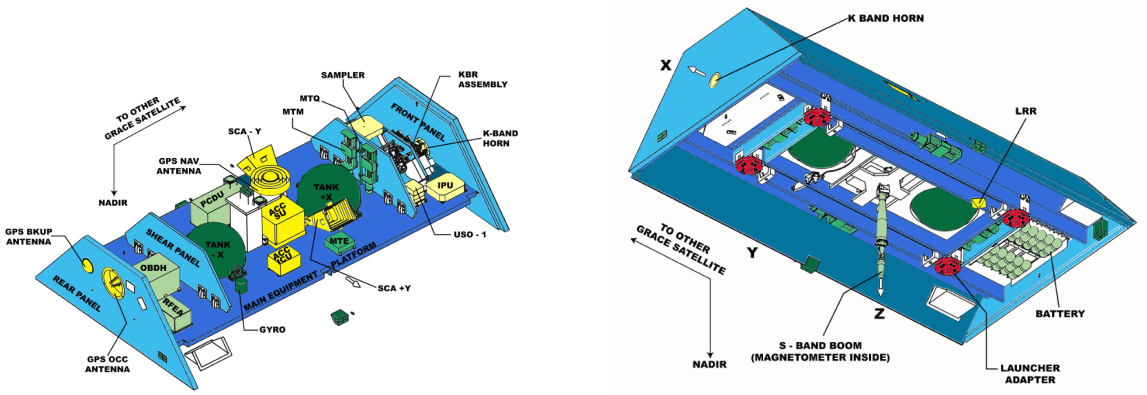

(a) Internal view.

(b) Bottom view.

Figure 2.1: Schematic Layout of a single GRACE-Satellite. (Source: `http://op.gfz-potsdam.de/grace/satellite/satellite.html`)

as an occultation antenna which allows the determination of vertical temperature and humidity profiles.

SuperSTAR Accelerometer The SuperSTAR accelerometer is an improved version of the accelerometer used in the CHAMP mission. It's main objective is the measurement of non-conservative forces acting on the satellite's surface such as drag, Earth's albedo and solar radiation pressure. To eliminate gravitational influences and to allow a clear separation between linear and angular accelerations, the instrument is mounted in the satellite's center of mass. To compensate for the fact that the center of mass changes with the amount of fuel spent, a MTM (Center of Mass Trim Assembly Mechanism) is installed.

Star Camara Assembly The SCA (Star Camara Assembly) allows an accurate determination of the satellite's attitude. It consists of two CCD-arrays mounted left and right of the zenith direction in a 45 degree angle. By comparing measured star constellation with pre-recorded catalogues, the attitude of the spacecraft can be derived. Since the K-band ranging system requires mutual line of sight between the satellites the SCA is essential for scientific operation. Furthermore the satellite's attitude is required to transform the non-conservative forces measured by the onboard accelerometer into the quasi-inertial reference frame.

Laser Retro Reflector The LRR (Laser Retro Reflector) provided by GFZ allows a GPS independent determination of the spacecraft's orbit for backup and verification purposes by means of SLR (Satellite Laser Ranging).

2.2 Temporal Aliasing

The temporal variations in Earth's gravity field are in general represented by a set of spherical harmonic coefficients for a given observation period. This is due to the fact that a homogeneous global data distribution is required for a stable computation of an unconstrained gravity field solution. In case of the GRACE mission, a data set spanning a time period of one month is needed to achieve this homogeneous distribution on the globe (see figure 2.2).

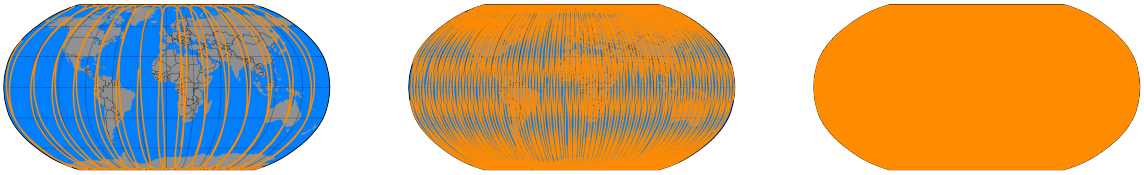

(a) 24 hours. (b) Seven days. (c) 31 days.

Figure 2.2: GRACE ground track coverage. A homogeneous data distribution is achieved after a continuous observation period of one month.

These gravity field solutions (in the following denoted *monthly solutions*) represent the temporal mean of the gravity field within the observation period, meaning that all temporal variations are implicitly assumed constant within this month. In reality however, processes which cause mass redistribution and therefore gravity field variations with a significantly higher frequency exist (c.f. Ilk et al., 2005). This leads to under-sampling of the time-variable gravity field signal which causes aliasing effects according to the Nyquist-Shannon theorem (e.g. Oppenheim et al., 1999). To avoid these aliasing errors, the observations are reduced by the application of geophysical models beforehand. These models contain Earth and Ocean tides as well as mass variations from atmosphere and ocean which are combined in the AOD1B (Atmosphere and Ocean De-aliasing Level-1B) product (Flechtner et al., 2014).
If these models contain errors or do not fully represent the complete mass variations, residual aliasing effects remain and deteriorate the gravity field solutions.
In Mayer-Gürr et al., 2010a it is shown that also unmodeled long term temporal variations have a major impact on monthly solutions and cause similar GRACE typical striping patterns than the undersampling of the time variable gravity field signal.
It is therefore essential to find an appropriate integrated representation of the Earth's static and time variable gravity field to obtain reliable estimates.

3 Representation of the Time Variable Gravity Field

Due to the fact that Earth's gravity field is subject to temporal variations caused by mass transport and deformation, a suitable modeling of such changes is necessary when performing gravity field recovery from satellite data. This section deals with the mathematical representation of the static and time variable gravity field and lists typically used mathematical models in gravity field recovery.
A popular representation of the static gravity field component is the expansion of the potential into a spherical harmonic series (Heiskanen and Moritz, 1967):

$$V(r,\vartheta,\lambda) = \frac{GM}{R}\sum_{n=0}^{\infty}\left(\frac{R}{r}\right)^{n+1}\sum_{m=-n}^{N} a_{nm}Y_{nm}(\vartheta,\lambda). \tag{3.1}$$

The scale factor $\frac{GM}{R}$ consisting of the geocentric gravitational constant and a reference radius, is introduced for numerical reasons. The basis functions Y_{nm} are Laplacian surface spherical harmonics in the form of

$$Y_{nm}(\vartheta,\lambda) = P_{nm}(\cos\vartheta)\begin{cases}\cos m\lambda & \text{for} \quad m \geq 0\\ \sin m\lambda & \text{otherwise}\end{cases}, \tag{3.2}$$

with the fully-normalized Legendre-polynomials $P_{nm}(\cos\vartheta)$. The corresponding spherical harmonic coefficients a_{nm} with

$$a_{nm} = \begin{cases}c_{nm} & \text{for} \quad m \geq 0\\ s_{nm} & \text{otherwise}\end{cases}. \tag{3.3}$$

3.1 Mathematical Modeling of Temporal Variations

To gain flexibility in modeling temporal variations of Earth's gravity field a generalization to arbitrary basis functions in the time domain is desirable. One can view the time-variable gravity field as sum of gravitational variations caused by mass distribution in the Earth's system. Mathematically this can be expressed as a linear combination of basis functions in time domain

$$V(r,\vartheta,\lambda,t) = \sum_{k=0}^{\infty} f_k(r,\vartheta,\lambda)\cdot\Phi^{(k)}(t). \tag{3.4}$$

Equation (3.4) can be interpreted as a potential time series for each point in space. The spatially dependent coefficients f_i can be expressed in analogy to the static gravity field as

$$f_k(r,\vartheta,\lambda) = \frac{GM}{R}\sum_{n=0}^{\infty}\left(\frac{R}{r}\right)^{n+1}\sum_{m=-n}^{N} a_{nm}^{(k)}Y_{nm}(\vartheta,\lambda), \tag{3.5}$$

where $a_{nm}^{(k)}$ are the set of spherical harmonic coefficients corresponding to the temporal basis function $\Phi^{(k)}$ and the spatial basis function Y_{nm}.
The monthly block means typically used for GRACE gravity field solutions can be seen as special case of equation (3.4). In this case, a zero degree basis spline with support of one

month is used as basis function for each set of potential coefficients (see figure 3.1). Other examples include quadratic splines as temporal basis functions (Mayer-Gürr et al., 2010a) which allow a continuous temporal representation, or secular, annual and semi-annual variations (e.g. EIGEN-6, Förste et al., 2011).

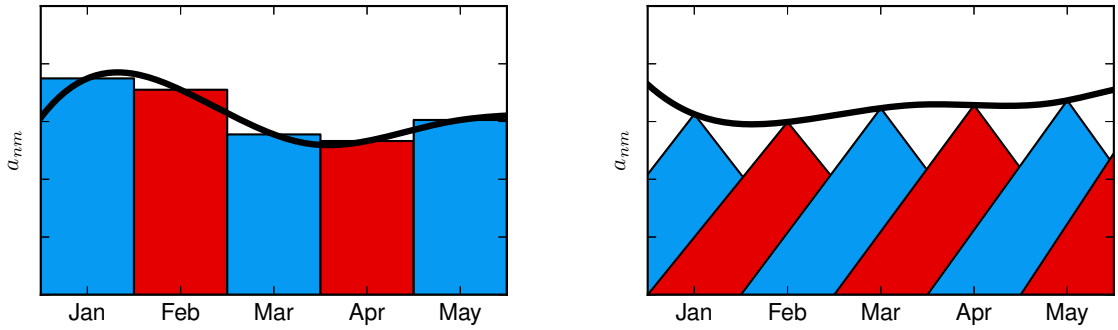

(a) Zero degree spline.

(b) First degree spline.

Figure 3.1: Representation of Earth's gravity field using basis splines.

3.2 Kalman-Filter Approach

To reduce aliasing errors, an increase of the temporal sampling rate an therefore shorter time periods in which the Earth's gravity field is assumed constant, is desirable. Furthermore, higher temporal resolution also allows the detection and measurement of unmodeled physical processes with higher frequency in time domain. Since the ground-track coverage of GRACE does not allow a stable daily gravity field solution, Kurtenbach et al., 2009 proposed a Kalman-filter (e.g. Kalman, 1960 or Welch and Bishop, 2006) approach to overcome this limitation. An improved procedure was investigated and presented in Kurtenbach, 2011 and shall be outlined in the following paragraphs.
The basic principle in the Kalman-filter approach lies in the fact that Earth's gravity field does not change arbitrarily over time but follows the mass redistributions caused by geophysical processes. Using models which describe these processes one can derive an empirical model which provides a state-transition matrix $\mathbf{B}$ linking two consecutive days like

$$\mathbf{x}_{t+1} = \mathbf{B}\mathbf{x}_t + \mathbf{w} \quad \text{with} \quad \mathbf{w} \sim \mathcal{N}(0, \mathbf{Q}). \tag{3.6}$$

This represents a prediction of the gravity field from day t to the next day $t+1$, with the noise vector $\mathbf{w}$ describing the accuracy of the prediction. In Kurtenbach, 2011 the state-transition matrix is derived using least-squares prediction (for example Moritz, 1980) based on the empirical auto-covariance and cross-covariance matrices of the expected signal

$$\mathbf{B} = \mathbf{\Sigma}^{-1}\mathbf{\Sigma}_{\Delta}. \tag{3.7}$$

The covariance matrix of the process noise vector $\mathbf{Q}$ can be derived by applying covariance propagation to (3.6) with $\mathcal{C}(x_{t+1}) = \mathcal{C}(x_t) = \mathbf{\Sigma}$, which leads to

$$\mathbf{Q} = \mathbf{\Sigma} - \mathbf{\Sigma}_{\Delta}\mathbf{\Sigma}^{-1}\mathbf{\Sigma}_{\Delta}^{T}. \tag{3.8}$$

Using GRACE observations the prediction in (3.6) can be improved. This is done within the Kalman-filter update-step which in essence performs a weighted combination of pseudo-observations represented by the predicted state and the state estimated from GRACE observations (Kurtenbach et al., 2012). Figure 3.2 outlines the two step prediction-update cycle of the Kalman-filter.

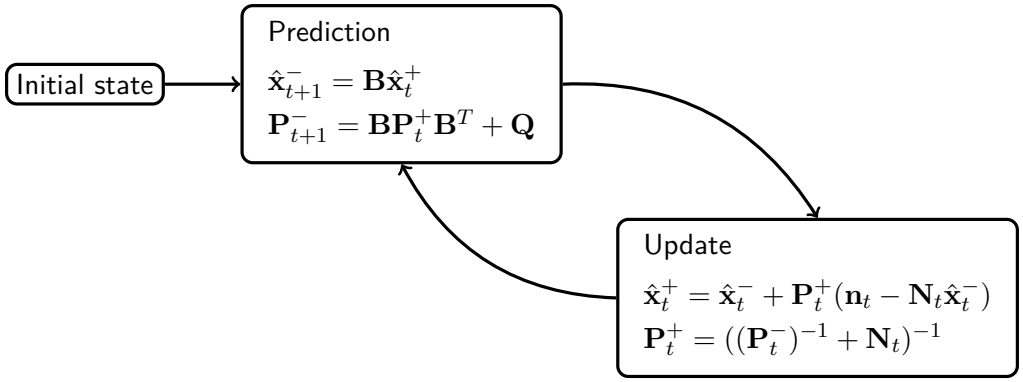

Figure 3.2: Schematic principle of the two-step Kalman-filter procedure (Adapted from Kurtenbach et al., 2012). Quantities with a minus as superscript ($\hat{\mathbf{x}}^{-}$, $\mathbf{P}^{-}$) describe the a-priori state estimate which only depends on the process dynamic. The a-posteriori state estimate is denoted by a +-superscript ($\hat{\mathbf{x}}^{+}$, $\mathbf{P}^{+}$).

The daily gravity field snapshots derived with this Kalman-filter approach were used as improved dealiasing product in the computation of the ITG-Grace2010 gravity field model (Mayer-Gürr et al., 2010b). This was done in a two step procedure wherein the first step the time series of daily gravity field solutions was computed. In the next step these gravity field snapshots were reduced from the GRACE-L1B data in form of an improved dealiasing product. This reduced data set was then used in the estimation of the monthly block means and the static gravity field ITG-Grace2010s (Mayer-Gürr et al., 2010b).

4 Setting up the Observation Equations

4.1 Precise Orbit Determination

Both GRACE satellites carry a GPS receiver on board to acquire satellite-to-satellite tracking data in the high-low configuration (SST-hl). These phase and code measurements are used to determine the position of the satellites along their respective orbits by means of POD, see for example Zehentner and Mayer-Gürr, 2013. In case of the GRACE mission, these observations establish the basis of the functional model and serve as complementary observations to the K-band observables.
Popular uses for POD measurements in the context of gravity field recovery are the acceleration approach as proposed by Austen and Reubelt, 2000, the acceleration approach via double differences, as introduced by Ditmar and Eck van der Sluijs, 2004 and the energy integral (O'Keefe, 1957, Bjerhammar, 1967, Reigber, 1969 and Ilk and Löcher, 2003). In the following only the method actually used for the computations in this thesis will be discussed in detail. It is based on an integration equation which was first proposed for orbit computation in Schneider, 1968 and later tailored to gravity field determination by Reigber, 1969. The first successful application of this method in the space domain was executed by Mayer-Gürr et al., 2005 and resulted in the global CHAMP gravity field ITG-CHAMP01. The following short overview of the integral equation approach is a summary of Mayer-Gürr, 2006, chapter 4.
The relation between the motion of a satellite along it's orbit and the acting forces is defined via Newton's equation of motion, here formulated with respect to the unit mass:

$$\ddot{\mathbf{r}}(t) = \mathbf{f}(t, \mathbf{r}, \dot{\mathbf{r}}), \tag{4.1}$$

with $\ddot{\mathbf{r}}(t)$ denoting the satellite's acceleration at a given time t, $\mathbf{r}$ describing the satellite's position and $\dot{\mathbf{r}}$ describing the spacecraft's velocity. In practice, this differential equation is non-linear because the force function $\mathbf{f}$ does not depend linearly on the satellite's position. Integrating (4.1) twice and introducing the boundary values $\mathbf{r}_A$ and $\mathbf{r}_B$ with

$$\mathbf{r}_A := \mathbf{r}(t_A) \quad \text{and} \quad \mathbf{r}_B := \mathbf{r}(t_B), \quad t_A < t_B \tag{4.2}$$

for the satellite's position at the beginning and end of an arc along its orbit, results in an integral equation for the satellite position formulated as boundary value problem.
Introducing the normalized time with a domain of $[0, 1]$

$$\tau = \frac{t - t_A}{T} \quad \text{with} \quad T = t_B - t_A, \tag{4.3}$$

and the integral kernel

$$K(\tau, \tau') = \begin{cases} (1-\tau')\tau & \text{if } \tau \leq \tau' \\ (1-\tau)\tau' & \text{if } \tau > \tau' \end{cases}, \tag{4.4}$$

the solution to (4.1) can be written as

$$\mathbf{r}(\tau) = (1-\tau)\mathbf{r}_A + \tau\mathbf{r}_B - T^2 \int_{\tau'=0}^{1} K(\tau, \tau')\mathbf{f}(\tau', \mathbf{r}, \dot{\mathbf{r}})d\tau'. \tag{4.5}$$

Equation 4.5 is a Fredholm type integral equation of the second kind. The unknowns are the boundary values $\mathbf{r}_A$ and $\mathbf{r}_B$ as well as the specific force function $\mathbf{f}(\tau', \mathbf{r}, \dot{\mathbf{r}})$ along the satellite's orbit arc. Since the satellite's orbit is observed and therefore contains measurement noise, the true positions $\mathbf{r}$ are substituted by the positions $\mathbf{r}_\epsilon$ derived from GPS. When dealing with POD observations, they can be assumed as sufficiently accurate, as has been shown in Mayer-Gürr, 2006. This means, the dependency of the force function on the unknown satellite orbit can be neglected. However, if the same equation is used to derive observation equations for the highly accurate K-band measurements, this dependency has to be taken into account, as will be described in section 4.2. The satellite's velocity $\dot{\mathbf{r}}$ only influences the force function due to non-conservative forces acting on the satellite surface, for example drag or solar radiation pressure. Those forces can be determined directly via the accelerometer on board each spacecraft, meaning the dependency of the force function on $\dot{\mathbf{r}}$ can be neglected as well. Taking the approximations described above into account, the simplified integral equation for POD observations then reads

$$\mathbf{r}(\tau) = (1-\tau)\mathbf{r}_A + \tau\mathbf{r}_B - T^2 \int_{\tau'=0}^{1} K(\tau, \tau')\mathbf{f}(\tau')d\tau'. \tag{4.6}$$

In practice, equation (4.6) is evaluated at each epoch τ_k within an arc along the satellite's orbit where an observation was taken. Arranging all epochs as a column vector in the form of

$$\mathbf{l} = \begin{bmatrix} \mathbf{r}(\tau_1) \\ \vdots \\ \mathbf{r}(\tau_N) \end{bmatrix}, \tag{4.7}$$

leads to an equation system relating the observations $\mathbf{l}$ to the boundary values $\mathbf{b} = [\mathbf{r}_A\ \mathbf{r}_B]^T$ and the integrated force function $\mathbf{h}$.

$$\mathbf{l} = \mathbf{B}\mathbf{b} + \mathbf{h} \tag{4.8}$$

In detail, the matrix $\mathbf{B}$ in equation (4.8) contains the normalized observation time for each epoch,

$$\mathbf{B} = \begin{bmatrix} (1-\tau_1) & \tau_1 \\ (1-\tau_2) & \tau_2 \\ \vdots & \vdots \\ (1-\tau_N) & \tau_N \end{bmatrix} \tag{4.9}$$

and the vector $\mathbf{h}$ consists of the integral in eq. (4.6) evaluated for each of the N observation epochs

$$\mathbf{h} = \begin{bmatrix} \mathbf{h}(\tau_1) \\ \vdots \\ \mathbf{h}(\tau_N) \end{bmatrix} \quad \text{with} \quad \mathbf{h}(\tau_k) = -T^2 \int_0^1 K(\tau_k, \tau')\mathbf{f}(\tau')d\tau'. \tag{4.10}$$

To form a linear relation between the observations in $\mathbf{l}$ and the unknown parameters $\mathbf{x}$, expression (4.10) is expanded as Taylor-series with respect to $\mathbf{x}$ and linearized by omitting higher order terms:

$$\mathbf{h} = \mathbf{h}_0 + \mathbf{A}\mathbf{x}. \tag{4.11}$$

A contains the partial derivatives of (4.10) with respect to the unknown parameters,

$$(\mathbf{A})_{ij} = \frac{\partial \mathbf{h}(t_i)}{\partial x_j}. \tag{4.12}$$

Substituting (4.11) into (4.8) leads to the linear system of observation equations

$$\mathbf{l} - \mathbf{h}_0 = \mathbf{B}\mathbf{b} + \mathbf{A}\mathbf{x}, \tag{4.13}$$

with the vector of unknown parameters as described in section 5. Since **h** is not directly dependent on the unknown parameters, but implicitly via the specific force function **f**, the elements of **A** have to be derived by applying the chain rule.

$$(\mathbf{A})_{ij} = \frac{\partial \mathbf{h}(\tau_i)}{\partial x_i} = \frac{\partial \mathbf{h}(\tau_i)}{\partial \mathbf{f}(\tau')} \frac{\partial \mathbf{f}(\tau')}{\partial x_i} \tag{4.14}$$

By expressing the partial derivatives in matrix notation like

$$(\mathbf{K})_{ij} = \frac{\partial \mathbf{h}(\tau_i)}{\partial \mathbf{f}(\tau'_j)} \quad \text{and} \quad (\mathbf{G})_{ji} = \frac{\partial \mathbf{f}(\tau'_j)}{\partial x_i} \tag{4.15}$$

equation (4.14) can be rewritten as

$$\mathbf{A} = \mathbf{K}\mathbf{G}. \tag{4.16}$$

The specific forces along the satellite's orbit can then be expressed using the unknown gravity field functionals according to

$$\begin{bmatrix} \mathbf{f}(\tau_1) \\ \vdots \\ \mathbf{f}(\tau_N) \end{bmatrix} = \mathbf{G}\mathbf{x} + \mathbf{a}, \tag{4.17}$$

where **a** represents the reference gravity field, tidal accelerations and the non-conservative surface forces measured by the onboard accelerometer. The observation vector **l** is later reduced by this vector which implies that all constituents of **a** are assumed error-free. Matrix **K** represents the integrator used to solve the integral in equation (4.10). Using quadrature methods, the linear relationship between **h** and **f** can be established. For a detailed description of the computation of **K** the reader is referred to Mayer-Gürr, 2006.
The reduction vector $\mathbf{h}_0$ in (4.13) is obtained by applying the integrator **K** to the reference accelerations **a**:

$$\mathbf{h}_0 = \mathbf{K}\mathbf{a}. \tag{4.18}$$

Substituting (4.16) and (4.18) into (4.13) leads to the Gauss-Markoff model,

$$\mathbf{l} - \mathbf{K}\mathbf{a} = \mathbf{K}\mathbf{G}\mathbf{x} + \mathbf{B}\mathbf{b} + \mathbf{e} \tag{4.19}$$

where **b** and **x** are the unknown parameters and **e** denotes the residual vector.

4.2 Low-Low Satellite Tracking

As indicated in the previous section, the functional model for processing POD measurements cannot be directly used for K-band observations. Due to the high accuracy of the observed intersatellite ranges, a highly accurate observation model is required for a sensible gravity field solution. The biased ranges between the two GRACE satellites can be determined with an accuracy of a few μm, which means that the model has to be significantly more accurate. This means that the model errors introduced by the simplification of the functional model (e.g. omission of position dependency), approximation by linearization or numerical influences such as the choice of numerical integrator have to be critically reviewed. The linearization error can be overcome by choosing good approximation values or by iteration of the estimation procedure. Numerical integration is also non-critical which was shown by Mayer-Gürr, 2006. The accuracy of the satellite's position that are introduced into the functional model however prove to be more problematic. In the integral equation (4.5) the force function $\mathbf{f}$ is evaluated at the specific satellite position corresponding to the observation epochs. When dealing with POD observations the inaccuracies of GPS positions were neglected, but this is no longer possible when dealing with intersatellite ranges. While the orbit position determined by GPS lies in the accuracy of a few centimeters, this is not sufficient for the functional model for highly precise K-band measurements. Mayer-Gürr, 2006 therefore proposed a refinement procedure for SST-ll observation equations. The basic outline of this method is described in the following. In reality the integral (4.5) is evaluated at noisy positions $\mathbf{r}_\epsilon$, resulting in perturbed positions $\hat{\mathbf{r}}$,

$$\hat{\mathbf{r}}(\tau) = (1-\tau)\mathbf{r}_A + \tau\mathbf{r}_B - T^2 \int_{\tau'=0}^{1} K(\tau,\tau')\mathbf{f}(\tau', \mathbf{r}_\epsilon, \dot{\mathbf{r}})d\tau'. \tag{4.20}$$

The difference to the true positions $\mathbf{r}$ can be calculated via

$$\mathbf{r}(\tau) - \hat{\mathbf{r}}(\tau) = T^2 \int_{\tau'=0}^{1} K(\tau,\tau')[\mathbf{f}(\tau', \mathbf{r}, \dot{\mathbf{r}}) - \mathbf{f}(\tau', \mathbf{r}_\epsilon, \dot{\mathbf{r}})]d\tau'. \tag{4.21}$$

By introducing the linear integral operator $\mathcal{K}(\cdot) = T^2 \int_0^1 K(\tau,\tau')(\cdot)d\tau'$ equation (4.21) can be rewritten in a simplified version as

$$\mathbf{r} - \hat{\mathbf{r}} = \mathcal{K}[\mathbf{f}(\mathbf{r}) - \mathbf{f}(\mathbf{r}_\epsilon)]. \tag{4.22}$$

Linearizing the specific force function as

$$\mathbf{f}(\mathbf{r}) = \mathbf{f}(\mathbf{r}_\epsilon) + \nabla\mathbf{f} \mid_{\mathbf{r}_\epsilon} (\mathbf{r} - \mathbf{r}_\epsilon) + \dots \tag{4.23}$$

and substituting (4.23) into (4.22), the difference between true and perturbed positions reads

$$\mathbf{r} - \hat{\mathbf{r}} = \mathcal{K}\nabla \mid_\epsilon (\mathbf{r} - \mathbf{r}_\epsilon)]. \tag{4.24}$$

Introducing the perturbed positions $\hat{\mathbf{r}}$ as expressed in (4.24) into the integral equation (4.20) leads to

$$[\mathcal{I} - \mathcal{K}\nabla\mathbf{f}(\mathbf{r}_\epsilon)] \underbrace{(\mathbf{r} - \mathbf{r}_\epsilon)}_{=\Delta\mathbf{r}} = \mathcal{K}\mathbf{f}(\mathbf{r}_\epsilon) + \underbrace{(1-\tau)\mathbf{r}_A + \tau\mathbf{r}_B}_{=\mathbf{b}} - \mathbf{r}_\epsilon. \tag{4.25}$$

In the discrete case, equation (4.25) can be expressed in matrix-vector notation in analogy to the POD observation equations as

$$[\mathbf{I} - \mathbf{KT}]\Delta\mathbf{r} = \mathbf{Kf}(\mathbf{r}_\epsilon) + \mathbf{Bb} - \mathbf{r}_\epsilon, \tag{4.26}$$

where $\mathbf{T}$ is a block-diagonal matrix containing the gravitational gradients for each epoch,

$$\mathbf{T} = \begin{bmatrix} \nabla\mathbf{f}(\tau_1) & & 0 \\ & \ddots & \\ 0 & & \nabla\mathbf{f}(\tau_N) \end{bmatrix}. \tag{4.27}$$

The assembly of matrix $\mathbf{T}$ in (4.27) requires a reference gravity field for the computation of $\nabla\mathbf{f}(\tau)$. A maximum spherical harmonic degree of $n_{\max} = 2$ to $n_{\max} = 3$ is sufficient in this refinement process as is shown in Mayer-Gürr, 2006.
Solving (4.26) for $\Delta\mathbf{r}$ leads to the position refinement vector $\Delta\mathbf{r}$ from which the unperturbed positions $\mathbf{r}$ used for the evaluation of the force function $\mathbf{f}$ can be obtained via

$$\mathbf{r} = \mathbf{r}_\epsilon + \Delta\mathbf{r}. \tag{4.28}$$

To apply the refined model for positions to intersatellite ranges ρ, the relative distance between the satellites is projected onto the line-of-sight vector

$$\rho(\tau) = \mathbf{e}_{12}(\tau) \cdot (\mathbf{r}_2(\tau) - \mathbf{r}_1(\tau)). \tag{4.29}$$

The vectors $\mathbf{r}_1(\tau)$ and $\mathbf{r}_2(\tau)$ in (4.29) represent the position of both satellites at the epoch τ and $\mathbf{e}_{12}(\tau)$ is the unit vector of the line-of-sight with

$$\mathbf{e}_{12}(\tau) = \frac{\mathbf{r}_2(\tau) - \mathbf{r}_1(\tau)}{\|\mathbf{r}_2(\tau) - \mathbf{r}_1(\tau)\|}. \tag{4.30}$$

Analog expressions for range-rates and range-accelerations can be found in Mayer-Gürr, 2006.
To obtain a linear relation between the intersatellite observable $\rho(\tau)$ and the unknown parameters $\mathbf{x}$, equation (4.29) has to be developed into a Taylor-series as

$$\rho = \rho_0 + \frac{\partial\rho}{\partial\mathbf{x}} \,|_{\mathbf{x}_0}\, \Delta\mathbf{x} + \dots. \tag{4.31}$$

Since ρ does not directly depend on $\mathbf{x}$, the chain rule has to be applied. In a first step, the ranges are differentiated with respect to the satellite positions $\mathbf{r}$. Then, the satellite positions are differentiated with respect to the force function $\mathbf{f}$ and in a final step the force function is differentiated with respect to the unknown parameters, leading to

$$\frac{\partial\rho}{\partial\mathbf{x}} = \frac{\partial\rho}{\partial\mathbf{r}_1}\frac{\partial\mathbf{r}_1}{\partial\mathbf{f}}\frac{\partial\mathbf{f}}{\partial\mathbf{x}} + \frac{\partial\rho}{\partial\mathbf{r}_2}\frac{\partial\mathbf{r}_2}{\partial\mathbf{f}}\frac{\partial\mathbf{f}}{\partial\mathbf{x}}. \tag{4.32}$$

The partial derivatives of ρ with respect to $\mathbf{r}_1$ and $\mathbf{r}_2$ yield the unit vector $-\mathbf{e}_{12}$ and $\mathbf{e}_{12}$ respectively, which means (4.32) can be interpreted as the projection of the observation equations (4.19) into the satellite line-of-sight.

5 Solving the Overdetermined Equation System

As outlined in section 4, the linear relation between the satellite measurements and the unknown parameters can be expressed as an equation system in the form of

$$\mathbf{l} = \mathbf{A}\mathbf{x} + \mathbf{e} \qquad \text{with} \qquad \mathcal{C}(\mathbf{e}) = \sigma^2 \mathbf{P}^{-1}. \tag{5.1}$$

Since the observations taken are subject to random measurement errors, the equation is generally not consistent and therefore not solvable in a straightforward way. Through addition of a random residual vector $\mathbf{e}$ representing the errors in the observations, a consistent equation system can be obtained (e.g. Koch, 2004 or Niemeier, 2008). This results in the general form of the *Least-Squares Adjustment* in equation (5.1).
Applying the fundamental condition of a minimum-norm residual vector to equation (5.1) leads to the so-called normal equations,

$$\mathbf{N}\hat{\mathbf{x}} = \mathbf{n} \qquad \text{where} \qquad \mathbf{N} = \mathbf{A}^T\mathbf{P}\mathbf{A} \qquad \text{and} \qquad \mathbf{n} = \mathbf{A}^T\mathbf{P}\mathbf{l}, \tag{5.2}$$

which yields a best, unbiased estimation of the unknown parameters (Koch, 2004).
When dealing with problems in the field of satellite geodesy, the number of observations as well as the number of unknown parameters is usually large, leading to problems in the practical evaluation of the least-squares adjustment due to computer memory restrictions.
The following example shall outline the memory requirements for a GRACE gravity field solution with additionally modeled daily variations, based on the short arc approach described in chapter 4.

Example 5.1: Memory requirement for a GRACE solution over the time span of one year with daily variations.
Given the sampling rate of the K-Band measurements of 5 s, approximately 6,420,000 observations are taken in the time span of 365 days. Per day, 16 state vectors for each satellite as well as 1677 spherical harmonic coefficients representing the daily gravity field variations are estimated. Adding the static representation of the monthly gravity field (spherical harmonic coefficients up to degree 180) a total of 714,946 parameters is obtained.
Using double precision floating point numbers (8 byte per number) the normal equation system of this gravity field solution requires 3.8 Tb of system memory, and the corresponding observation equations required a total of 34.2 Tb of available system memory when fully assembled. The full variance-covariance matrix of the correlated observations would require $1.5 \cdot 10^{14}$ Tb.

As example 5.1 shows, some considerations have to be made to solve the overdetermined equation system (5.1) in a sensible time frame. When, for example, only the long-term mean gravity field is of interest, the short-term variations and satellite specific parameters can be eliminated beforehand (see section 5.3). Furthermore, the assembly of the full variance co-variance matrix of observations can be avoided by transforming the residuals in the process of decorrelation and homogenization (section 5.1). The design matrix and observation vector can be split into smaller intervals and later accumulated to form the normal equations for the desired time span, which also constitutes a simple entry point for the distribution of the problem within a parallel computing environment.

5.1 Decorrelation and Homogenization

To avoid the multiplication with the weight matrix $\mathbf{P}$ in the assembly of the normal equations, the structure of the variance-covariance matrix of the observations can be exploited.

Since the covariance matrix of observations $\mathbf{\Sigma}$ typically is symmetric and positive definite its Cholesky-decomposition can be computed:

$$\mathbf{\Sigma} = \sigma^2 \mathbf{P}^{-1} \quad \text{and} \quad \mathbf{P}^{-1} = \mathbf{W}^T \mathbf{W}, \tag{5.3}$$

where $\mathbf{W}$ is an upper triangular matrix.
By applying $\mathbf{W}^{-T}$ to the residual vector $\mathbf{e}$ one obtains the so called decorrelated residuals (e.g. Koch, 2004) in the form of

$$\bar{\mathbf{e}} = \mathbf{W}^{-T} \mathbf{e}. \tag{5.4}$$

Solving equation (5.1) for $\mathbf{e}$ and substituting the residual vector in equation (5.4) leads to the decorrelated Gauss-Markoff model

$$\mathbf{W}^{-T} \mathbf{l} = \mathbf{W}^{-T} \mathbf{A} \mathbf{x} + \mathbf{W}^{-T} \mathbf{e}, \tag{5.5}$$

or in a more compact notation

$$\bar{\mathbf{l}} = \bar{\mathbf{A}} \mathbf{x} + \bar{\mathbf{e}} \quad \text{with} \quad \mathcal{C}(\bar{\mathbf{e}}) = \sigma^2 \mathbf{I}. \tag{5.6}$$

From a computational point of view it is important to note that the explicit inverse of $\mathbf{W}^T$ is not computed but equation (5.5) is treated as triangular linear equation system. This allows for the computation of $\bar{\mathbf{e}}$, $\bar{\mathbf{l}}$ and $\bar{\mathbf{A}}$ via forward substitution.
The fact that $\mathcal{C}(\bar{\mathbf{e}}) = \sigma^2 \mathbf{I}$ holds can be verified by applying variance-covariance propagation to (5.4).

5.2 Accumulation of Observation Equations

The functional model for KBR and POD measurements as described in chapter 4 yields observation equations on a per-arc basis. To compute a gravity field solution for a longer time span the, individual arcs are assembled in an observation vector and corresponding composite design matrix like

$$\mathbf{l} = \begin{bmatrix} \mathbf{l}_1 \\ \mathbf{l}_2 \\ \vdots \\ \mathbf{l}_N \end{bmatrix} \quad \text{and} \quad \mathbf{A} = \begin{bmatrix} \mathbf{A}_1 \\ \mathbf{A}_2 \\ \vdots \\ \mathbf{A}_N \end{bmatrix}. \tag{5.7}$$

Furthermore, when working in a parallel computing environment, it is beneficent to distribute the computation of the observation equations among multiple processes. This not only reduces the memory requirements for each node, but also allows for balancing the computational load. It is therefore convenient to split the observation vector and the design matrix into smaller intervals.
A necessary condition for the accumulation of the complete normal equation matrix is that the intervals are not correlated. This means that the covariance matrix of the observations has to be block diagonal

$$\mathbf{\Sigma} = \begin{bmatrix} \mathbf{\Sigma}_1 & & & \\ & \mathbf{\Sigma}_2 & & \\ & & \ddots & \\ & & & \mathbf{\Sigma}_N \end{bmatrix}. \tag{5.8}$$

Substituting (5.7) and (5.8) into (5.2) with $\mathbf{P} = \mathbf{\Sigma}^{-1}$ then leads to the interval based accumulation via

$$\mathbf{N} = \sum_{k=1}^{N} \mathbf{A}_k^T \mathbf{\Sigma}_k^{-1} \mathbf{A}_k \quad \text{and} \quad \mathbf{n} = \sum_{k=1}^{N} \mathbf{A}_k^T \mathbf{\Sigma}_k^{-1} \mathbf{l}_k. \tag{5.9}$$

Equation (5.9) is not only useful when assembling the normal equation system from arc-wise observation equations, but also when accumulating normal equations for a long-term mean field from previously computed monthly normal equations. The matrix product $\mathbf{A}_k^T \mathbf{\Sigma}_k^{-1} \mathbf{A}_k$ and matrix-vector product $\mathbf{A}_k^T \mathbf{\Sigma}_k^{-1} \mathbf{l}_k$ is then replaced by the previously computed normal equations $\mathbf{N}_k$ and right hand side vector $\mathbf{n}_k$.

5.3 Elimination of Parameters

When dealing with gravity field recovery usually only the parameters representing the Earth's gravity field are of interest. The numerical values of auxiliary parameters such as sensor biases and satellite state vectors, on the other hand are of lesser interest.
This circumstance can be expressed in the adjustment process by splitting the design matrix and the parameter vector into gravity field and satellite specific parts. Applied to equation (5.1) this results in

$$\mathbf{l} = \mathbf{A}\mathbf{x} + \mathbf{B}\mathbf{y} + \mathbf{e}, \tag{5.10}$$

where $\mathbf{y}$ represents the parameter set of lesser interest, which will be eliminated to reduce the problem size. Forming the normal equations from the observation model in equation (5.10) leads to the blocked system

$$\begin{bmatrix} \mathbf{B}^T\mathbf{l} \\ \mathbf{A}^T\mathbf{l} \end{bmatrix} = \begin{bmatrix} \mathbf{B}^T\mathbf{B} & \mathbf{B}^T\mathbf{A} \\ \mathbf{A}^T\mathbf{B} & \mathbf{A}^T\mathbf{A} \end{bmatrix} \begin{bmatrix} \hat{\mathbf{y}} \\ \hat{\mathbf{x}} \end{bmatrix}. \tag{5.11}$$

Assuming $\mathbf{B}^T\mathbf{B}$ is invertible, the first equation in (5.11) can be solved for $\hat{\mathbf{y}}$ resulting in

$$\hat{\mathbf{y}} = (\mathbf{B}^T\mathbf{B})^{-1}\mathbf{B}\mathbf{l} - (\mathbf{B}^T\mathbf{B})^{-1}\mathbf{B}\mathbf{A}\hat{\mathbf{x}}. \tag{5.12}$$

Substituting (5.12) into (5.11) yields an equation system only containing $\hat{\mathbf{x}}$ as vector of unknowns

$$\mathbf{A}^T(\mathbf{I} - \mathbf{B}(\mathbf{B}^T\mathbf{B})^{-1}\mathbf{B}^T)\mathbf{l} = \mathbf{A}^T(\mathbf{I} - \mathbf{B}(\mathbf{B}^T\mathbf{B})^{-1}\mathbf{B}^T)\mathbf{A}\hat{\mathbf{x}}. \tag{5.13}$$

The expression

$$\mathbf{I} - \mathbf{B}(\mathbf{B}^T\mathbf{B})^{-1}\mathbf{B}^T, \tag{5.14}$$

forms a projector into the orthogonal space of the range of $\mathbf{B}$ (for example Koch, 2004). An efficient way of computing this orthogonal projector is provided by the QR-decomposition

(e.g. Golub and Van Loan, 1996 or Higham, 2002). $\mathbf{B}$ can be decomposed into a product of an orthogonal matrix $\mathbf{Q}$ and an upper trapezoidal matrix $\mathbf{R}$:

$$\mathbf{B} = \mathbf{QR} = \begin{bmatrix} \mathbf{Q}_1 & \mathbf{Q}_2 \end{bmatrix} \begin{bmatrix} \mathbf{R} \\ 0 \end{bmatrix}. \tag{5.15}$$

Substituting (5.15) into (5.14) and exploiting the orthogonality of $\mathbf{Q}$ yields

$$\mathbf{I} - \mathbf{B}(\mathbf{B}^T\mathbf{B})^{-1}\mathbf{B}^T = \mathbf{I} - \mathbf{Q}_1\mathbf{Q}_1^T = \mathbf{Q}_2\mathbf{Q}_2^T. \tag{5.16}$$

Using the relations in (5.14), the transformation of the Gauss-Markoff model which corresponds to the elimination of the parameter vector $\mathbf{y}$ can be performed by multiplying (5.10) with $\mathbf{Q}_2^T$ from the left:

$$\mathbf{Q}_2^T\mathbf{l} = \bar{\mathbf{l}}, \quad \mathbf{Q}_2^T\mathbf{A} = \bar{\mathbf{A}} \quad \text{and} \quad \mathbf{Q}_2^T\mathbf{e} = \bar{\mathbf{e}}. \tag{5.17}$$

Equations (5.11) and (5.13) can also be viewed from a normal equation standpoint, namely

$$\begin{bmatrix} \mathbf{n}_1 \\ \mathbf{n}_2 \end{bmatrix} = \begin{bmatrix} \mathbf{N}_{11} & \mathbf{N}_{12} \\ \mathbf{N}_{12}^T & \mathbf{N}_{22} \end{bmatrix} \begin{bmatrix} \hat{\mathbf{y}} \\ \hat{\mathbf{x}} \end{bmatrix}. \tag{5.18}$$

Performing the same steps as in (5.12) and (5.13) leads to

$$\mathbf{n}_2 - \mathbf{N}_{12}^T\mathbf{N}_{11}^{-1}\mathbf{n}_1 = (\mathbf{N}_{22} - \mathbf{N}_{12}^T\mathbf{N}_{11}^{-1}\mathbf{N}_{12})\hat{\mathbf{x}}, \tag{5.19}$$

which, in a more compact expression yields a normal equation system with only the desired vector of parameters $\mathbf{x}$ as unknowns

$$\bar{\mathbf{N}}\hat{\mathbf{x}} = \bar{\mathbf{n}} \quad \text{with} \quad \bar{\mathbf{N}} = \mathbf{N}_{22} - \mathbf{N}_{12}^T\mathbf{N}_{11}^{-1}\mathbf{N}_{12} \quad \text{and} \quad \bar{\mathbf{n}} = \mathbf{n}_2 - \mathbf{N}_{12}^T\mathbf{N}_{11}^{-1}\mathbf{n}_1. \tag{5.20}$$

An efficient way of performing the parameter elimination in (5.20) will be described in section 6.2.3.

5.4 Variance Component Estimation

When performing gravity field recovery typically a variety of different observation groups are used in the adjustment process. In GRACE processing for example a combination of KBR measurements as well as POD positions are used. On a broader scale, complementary satellite missions as well as terrestrial data can be used in a single least squares adjustment to provide high resolution gravity fields such as the EGM2008 (Pavlis et al., 2008) or GOCO03s (Mayer-Gürr et al., 2012). Furthermore, appropriate regularization parameters are required when introducing a-priori information into the adjustment process. In such cases, the appropriate weighting for each observation group is crucial to obtain reliable estimates. A popular tool to determine such relative weighting factors is the variance component estimation (VCE, e.g. Koch, 2004 or Niemeier, 2008).

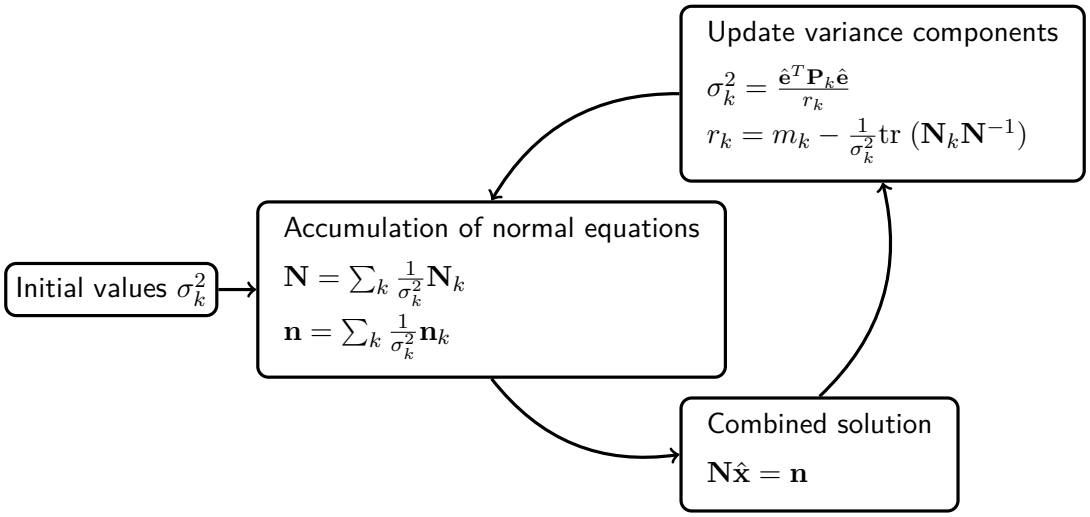

Figure 5.1: Schematic principle of the iterative variance component estimation procedure.

The general VCE procedure can be split into three major steps (e.g. Niemeier, 2008). As a first step, the normal equation matrices and right-hand-sides of each observation group are accumulated using initial values for the individual weighting factors σ_k^{-2}.

$$\mathbf{N}\hat{\mathbf{x}} = \mathbf{n} \quad \text{with} \quad \mathbf{N} = \sum_k \frac{1}{\hat{\sigma}_k^2} \mathbf{N}_k \quad \text{and} \quad \mathbf{n} = \sum_k \frac{1}{\hat{\sigma}_k^2} \mathbf{n}_k \tag{5.21}$$

The combined normal equation system is then solved, and an estimate of $\mathbf{x}$ is obtained allowing the computation of the norm of the residual vector $\hat{\mathbf{e}}_k^T \mathbf{P}_k \hat{\mathbf{e}}_k$ for each observation group. In the last step the variance components and corresponding group redundancies are updated:

$$\hat{\sigma}_k^2 = \frac{\hat{\mathbf{e}}_k^T \hat{\mathbf{e}}_k}{r_k} \quad \text{and} \quad r_k = n_k - \frac{1}{\sigma_k^2} \mathrm{tr}\,(\mathbf{N}_k \mathbf{N}^{-1}). \tag{5.22}$$

In practice the trace of $\mathbf{N}_k \mathbf{N}^{-1}$ is not computed directly but estimated via an efficient stochastic trace estimator (e.g. Kusche, 2002) This procedure is repeated until convergence is achieved (see figure 5.1).

6 Incorporation of Temporal Variations into the Adjustment Process

The following chapter deals with the formulation of observation and normal equations which allow the incorporation temporal variations into the gravity field recovery process. In the first section, the generalized representation of the time variable gravity field is applied to the functional models described in chapter 4.
In analogy to Kurtenbach, 2011, daily estimates of the gravity field have been modeled as a representation of short-term temporal variations. Section 6.1.1 deals with this special case which requires a-priori information for a reliable estimate. The functional model as well as the incorporation of pseudo-observations to stabilize the ill-posed problem are described in detail. The implementation of the previously derived mathematical relations for the modeling of temporal variations in the adjustment process is outlined in section 6.2.

6.1 Formulation of the Observational Model

Based on the mathematical representation of the time variable gravity field in 3.1 an observational model containing the static, as well as the time variable gravity field component can be derived. By introducing the gravitational part of the specific force function $\mathbf{f}$ as a linear combination of temporal basis functions according to (3.4), the following observational model is obtained:

$$l(t_i) = \sum_{k=0}^{m} \Phi^{(k)}(t_i)\mathbf{A}(t_i)\mathbf{x}^{(k)} + e(t_i). \tag{6.1}$$

In practice, the time variability of the Earth's gravity field is approximated by a finite number of time dependent basis functions m. Furthermore, the gravity field is assumed to be constant within a given interval $[t_i, t_{i+1})$ from which

$$\Phi^{(k)}(t) = \text{const} \quad \forall\, t \in [t_i, t_{i+1}) \tag{6.2}$$

follows. This does not only alleviate the computational implementation, but also reflects the fact that it is assumed that the variability of the gravity field is reduced after the application of the dealiasing products. In this thesis, the interval in which the gravity field after application of dealiasing product and background models is assumed constant, is chosen with one day in accordance to Kurtenbach, 2011. This approximation then allows the grouping of all observations in an equation system since the temporal factor Φ is constant for each observation within the given interval

$$\mathbf{l}_i = \sum_{k=0}^{m} \Phi_i^{(k)}\mathbf{A}_i\mathbf{x}^{(k)} + \mathbf{e}_i, \tag{6.3}$$

with the shorthand notation

$$\Phi^{(k)}(t_i) = \Phi_i^{(k)}, \qquad \mathbf{A}(t_i) = \mathbf{A}_i \qquad \mathbf{l}(t_i) = \mathbf{l}_i \text{ and} \qquad \mathbf{e}(t_i) = \mathbf{e}_i. \tag{6.4}$$

Applying (6.3) to the whole observation period then leads to the full observation equation system containing each interval $\mathbf{l}_i$

$$\begin{bmatrix} \mathbf{l}_1 \\ \mathbf{l}_2 \\ \vdots \\ \mathbf{l}_N \end{bmatrix} = \begin{bmatrix} \Phi_1^{(0)}\mathbf{A}_1 & \Phi_1^{(1)}\mathbf{A}_1 & \dots & \Phi_1^{(m)}\mathbf{A}_1 \\ \Phi_2^{(0)}\mathbf{A}_2 & \Phi_2^{(1)}\mathbf{A}_2 & \dots & \Phi_2^{(m)}\mathbf{A}_2 \\ \vdots & \vdots & & \vdots \\ \Phi_N^{(0)}\mathbf{A}_N & \Phi_N^{(1)}\mathbf{A}_N & \dots & \Phi_N^{(m)}\mathbf{A}_N \end{bmatrix} \begin{bmatrix} \mathbf{x}^{(0)} \\ \mathbf{x}^{(1)} \\ \vdots \\ \mathbf{x}^{(m)} \end{bmatrix} + \begin{bmatrix} \mathbf{e}_1 \\ \mathbf{e}_2 \\ \vdots \\ \mathbf{e}_N \end{bmatrix}. \tag{6.5}$$

Due to the fact that the temporal variations are modeled as linear combinations of the spatial basis functions (c.f. equation (3.4)), the corresponding design matrix $\mathbf{A}_i$ can be used for each temporal factor $\Phi_i^{(k)}$. This proves to be convenient from a computational point of view, since the observation equations have to be only assembled once for any number m of temporal factors. During the assembly of the normal equations, this circumstance is also exploited to avoid unnecessary matrix operations.
The normal equations corresponding to (6.5) can be computed by accumulation of each interval in accordance to section 5.2. Applied to the functional model at hand, this leads to

$$\mathbf{N} = \sum_{i=1}^{N} \begin{bmatrix} \Phi_i^{(0)}\mathbf{A}_i^T \\ \Phi_i^{(1)}\mathbf{A}_i^T \\ \vdots \\ \Phi_i^{(m)}\mathbf{A}_i^T \end{bmatrix} \begin{bmatrix} \Phi_i^{(0)}\mathbf{A}_i & \Phi_i^{(1)}\mathbf{A}_i & \dots & \Phi_i^{(m)}\mathbf{A}_i \end{bmatrix}, \quad \mathbf{n} = \sum_{i=1}^{N} \begin{bmatrix} \Phi_i^{(0)}\mathbf{A}_i^T \\ \Phi_i^{(1)}\mathbf{A}_i^T \\ \vdots \\ \Phi_i^{(m)}\mathbf{A}_i^T \end{bmatrix} \mathbf{l}_i. \tag{6.6}$$

For a single normal equation block $\mathbf{N}^{(k,l)}$ which corresponds to the correlations between the parameter sets $\mathbf{x}^{(k)}$ and $\mathbf{x}^{(l)}$ follows

$$\mathbf{N}^{(k,l)} = \sum_{i=1}^{N} (\Phi_i^{(k)}\mathbf{A}_i^T)(\Phi_i^{(l)}\mathbf{A}_i) = \sum_{i=1}^{N} \Phi_i^{(k)}\Phi_i^{(l)}\mathbf{N}_i, \tag{6.7}$$

where $\mathbf{N}_i = \mathbf{A}_i^T\mathbf{A}_i$. In analogy to (6.7) the right-hand side for each parameter vector can be computed via

$$\mathbf{n}^{(k)} = \sum_{i=1}^{N} \Phi_i^{(k)}\mathbf{A}_i^T\mathbf{l}_i = \sum_{i=1}^{N} \Phi_i^{(k)}\mathbf{n}_i, \tag{6.8}$$

utilizing $\mathbf{n}_i$.

6.1.1 Parametrization of short-term Variations

In this thesis the short-term gravity field variations are represented as daily block means, which correspond to a zero degree B-spline with support of one day as temporal basis function. The corresponding temporal factor can therefore be expressed as

$$\Phi_i(t) = \begin{cases} 1 & \text{if } t \in [t_i, t_{i+1}) \\ 0 & \text{otherwise} \end{cases}. \tag{6.9}$$

Applying (6.9) to the general design matrix described in (6.5), leads to an observation equation system with diagonal structure, where the design matrix entries $\mathbf{A}_i$ form the rectangular diagonal blocks.

$$\begin{bmatrix} \mathbf{l}_1 \\ \mathbf{l}_2 \\ \vdots \\ \mathbf{l}_N \end{bmatrix} = \begin{bmatrix} \mathbf{A}_1 & & & \\ & \mathbf{A}_2 & & \\ & & \ddots & \\ & & & \mathbf{A}_N \end{bmatrix} \begin{bmatrix} \mathbf{x}^{(1)} \\ \mathbf{x}^{(2)} \\ \vdots \\ \mathbf{x}^{(N)} \end{bmatrix} + \begin{bmatrix} \mathbf{e}_1 \\ \mathbf{e}_2 \\ \vdots \\ \mathbf{e}_N \end{bmatrix}. \tag{6.10}$$

Due to the fact that the GRACE ground-track coverage does not allow a stable recovery of daily gravity field solutions, a-priori information has to be introduced (e.g. Kurtenbach, 2011 or Kurtenbach et al., 2012). In analogy to the Kalman-filter approach developed in Kurtenbach, 2011, this is done in the form of spatial and temporal covariance matrices which describe the expected signal and its temporal evolution. The state-transition matrix $\mathbf{B}$ in (3.6) allows the formulation of the pseudo observations $\mathbf{l}$ with

$$\mathbf{l} = 0 = \mathbf{B}\mathbf{x}_t - \mathbf{x}_{t+1} + \mathbf{w} \quad \text{and} \quad \mathcal{C}(\mathbf{w}) = \mathbf{Q}, \tag{6.11}$$

which are used in the estimation process to regularize the ill-posed problem. Combining (6.10) and (6.11) then leads to the full observation equations for the short-term variations with

$$\begin{bmatrix} \mathbf{l}_1 \\ \mathbf{l}_2 \\ \vdots \\ \mathbf{l}_N \\ 0 \\ \vdots \\ 0 \end{bmatrix} = \begin{bmatrix} \mathbf{A}_1 & & & \\ & \mathbf{A}_2 & & \\ & & \ddots & \\ & & & \mathbf{A}_N \\ \mathbf{B} & -\mathbf{I} & & \\ & \ddots & \ddots & \\ & & \mathbf{B} & -\mathbf{I} \end{bmatrix} \begin{bmatrix} \mathbf{x}^{(1)} \\ \mathbf{x}^{(2)} \\ \vdots \\ \mathbf{x}^{(N)} \end{bmatrix} + \begin{bmatrix} \mathbf{e}_1 \\ \mathbf{e}_2 \\ \vdots \\ \mathbf{e}_N \\ \mathbf{w} \\ \vdots \\ \mathbf{w} \end{bmatrix}. \tag{6.12}$$

Other regularization methods, such as Kaula-regularization (*Kaula's Rule of Thumb*, Kaula, 1966) can be introduced in a similar fashion, but are not considered in this thesis.

6.2 Parallel Assembly of the Normal Equations

As can be seen in example 5.1, the memory demand for the computation of normal equations containing temporal variations is significant. To reduce the problem size, parameter elimination and decorrelation as outlined in chapter 5 are applied during the normal equation assembly. Another measure to reduce the problem size is the splitting of the time span of interest into monthly intervals for which one normal equation system is computed. Each monthly normal equation is then accumulated as outlined in section 5.2, to obtain the complete normal equation matrix for the whole investigation period. Due to the still comparably large problem size, the assembly of the normal equations cannot be performed in a sensible time frame on a single computer. It is therefore necessary to find a parallel implementation which reduces the computation time and splits the memory demand among multiple nodes.
The algorithm for the computation of the normal equations for one month can be subdivided into four main tasks:

Observation equations As a first step, the observation equations for one sub-interval (e.g. one month) are computed. This is performed on a per-arc basis, where each process is assigned a set of arc numbers.

Normal equation computation/distribution Based on the previously computed observation equations, the normal equation blocks for the static part are formed. For each block the subset of processes which requires this block for further computations is determined and the matrix is broadcast within this subset.

Accumulation Each individual block is scaled with the corresponding temporal factors $\Phi(t_i)$ and added to the normal equation system according to (6.7).

Parameter elimination After full assembly of the normal equations, all parameters specific to this month (i.e. short-term variations and satellite parameters) are eliminated using an incomplete Cholesky factorization. The result is a smaller normal equation system consisting only of static and long-term variation parts which implicitly contain the short-term and satellite parameters.

Each of the tasks shall be described in detail in the following sections.

6.2.1 Computation of Observation Equations

The observation equations are computed on a per-arc basis as outlined in section 4. For an arc length of 90 minutes as used in this thesis, this means that the total number of arcs for one month is approximately 500, depending on data gaps. These 500 arcs are assigned to intervals which correspond to the time intervals assigned for the short term variations. Example 6.1 outlines the arc distribution based on the month January.

Example 6.1: Arc distribution for January based on 90 minute arcs and one day interval bins.

Given an arc length of 90 minutes each day consists of 16 observation arcs assuming no data gaps occur. For January this means that a total of 496 observation arcs result, which are to be assigned to 31 intervals corresponding to one day as is described in section 6.1.1. Table 6.1 shows the intervals and the arc numbers of the contained arcs.

Table 6.1: Arc distribution for January assuming 90 minute observation arcs and no data gaps.

Interval	Arcs
$\mathcal{I}_1$	0 - 15
$\mathcal{I}_2$	16 - 31
	$\vdots$
$\mathcal{I}_{31}$	480 - 495

The fact that the observation equations are computed on a per arc basis and the individual arcs are assumed to be independent, allows for a straightforward parallelization of the procedure. A good load balance can be achieved using a master-slave configuration wherein the master process assigns arc numbers to idle processes until the whole month is computed. This so called *dynamic scheduling* is realized in a two step procedure:

- as soon as a process starts idling (i.e. has no arcs assigned or has just finished computing the observation equations for one arc), a message is sent to the master process

- the master process then assigns the next arc to be computed to the idling process which in turn starts to compute the corresponding observation equations.

To reduce the communication cost during the next step (forming the normal equations for each interval), it is beneficial to group all arcs of an interval on a single process or node. This follows directly from the fact that all arcs of interval $\mathcal{I}_i$ are required to form the normal equations according to (6.6). As a compromise between load balancing and the grouping of arcs on a single process, a constraint is introduced which minimizes the number of intervals for each process as long as arcs in these intervals remain to be computed.
The implementation of this dynamic scheduling is outlined in algorithm 6.1.

Algorithm 6.1: Parallel computation of the observation equations for one month. The work load is distributed via a master-slave configuration wherein a master process assigns arc numbers to idling processes. A constraint is introduced to minimize the number of intervals $\mathcal{I}$ on each process.

Input:
N... number of intervals
P...number of processes

```
if master:
    s = n ∈ ℕ /* random seed for first iteration */
    for i = 0 : max(N, P):
        j = (s + i)%N
        receive rank r from idling process
        send first arc in I_j to r
        w(r, j)++; w(r − 1, j)++; w(r + 1, j)++ /* increase weight for
            interval j and neighbors on process r */
    while arcs remain:
        receive rank r from idling process
        find interval j with w(r, j) = max w(r, j)
        while I_j is empty:
            exclude I_j
            find interval j with w(r, j) = max w(r, j)
        send first arc in I_j to r
else:
    while arcs remain:
        receive arc number k from master
        compute A_k, l_k
        send rank r to master /* indicate idle state */
```

Algorithm 6.1 behaves as follows: In the initial loop iteration, the first set of intervals is assigned to the processes. In the second step, as long as unassigned arcs exist, each idling process is assigned arcs from the interval with the maximum weight for the process are assigned. If no arcs remain for this interval, it is excluded from further computations and an arc of the interval which now possesses the new maximum weight is sent to the process.

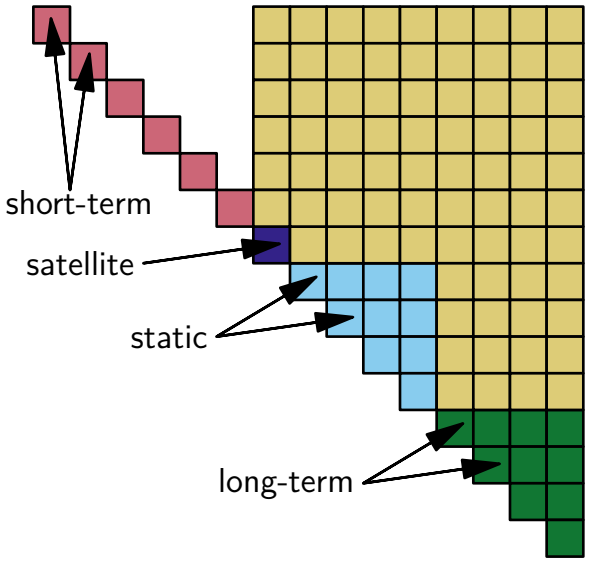

Figure 6.1: Normal equation structure for the combined equation system consisting of modelled short-term (daily), long-term (e.g. secular, annual) variations and static parts. Note that only the upper triangle is shown and stored. The proportion of the individual parts correspond to a static field up to degree and order 200, daily variations up to degree and order 40 and long-term variations (secular, sine and cosine coefficients for annual oscillation) modeled up to degree and order 120. The parameter order is chosen so that the structure of the matrix is preserved after application of the incomplete Cholesky algorithm.

6.2.2 Normal Equation Computation and Distribution

After computation of the observation equations, the normal equation structure is set up. As can be seen in figure 6.1, the parameter vector is essentially split into four different parameter groups. The first two groups consists of parameters modeled only for a certain time span, namely as short term variations and satellite specific parameters. These two groups will be denoted *epoch-dependent* parameters in the following sections. The third and fourth groups consists of modeled static field and long term variations which are set up for the whole observation period. A detailed reasoning for the parameter order indicated in figure 6.1 is given in section 6.2.3.

The design matrix $\mathbf{A}$ and the observation vector $\mathbf{l}$ are essentially distributed row-wise and the load dependent process to row mapping is random within the bounds of the introduced constraints. The normal equation matrix on the other hand is distributed according to a two-dimensional block-cyclic distribution (e.g. Blackford et al., 1997) on the processes. This is primarily done due to the fact that the parameter elimination is performed via an incomplete Cholesky decomposition. As is shown in Dongarra et al., 1992 the block-cyclic distribution provides good load balance for such decomposition algorithms. For the distribution among the process grid, the full normal equation matrix is subdivided into smaller block matrices which are then assigned to the individual processes. For the problem at hand, a blocking factor (block size) of 2048×2048 was chosen which means that the normal equation matrix corresponding to the static gravity field part (spherical harmonic coefficients up to d/o 200) consists of 20×20 block matrices.

Figure 6.2 shows the basic principle of the two-dimensional block-cyclic distribution on the basis of a quadratic 6×6 block matrix.

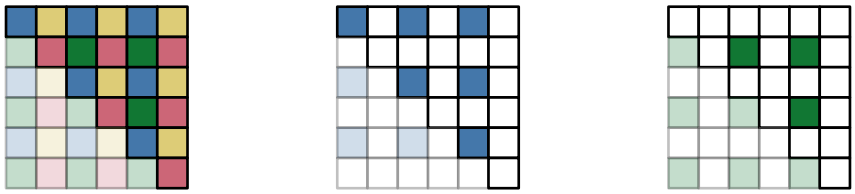

(a) Global view. (b) Local view of p_0. (c) Local view of p_1.

Figure 6.2: Global and local view of a matrix distributed on a 2×2 process grid. The individual processes p_i only allocate their respective blocks. In case of a symmetric or triangular matrix, only one triangle is allocated on the process grid as indicated by the transparent blocks.

Since the computation of the static normal equation matrix $\mathbf{N}_i$ requires a large amount of memory per node (a parametrization of spherical harmonic coefficients up to degree and order 200 requires about 6.7 Gb when storing one matrix triangle), considerations have to be made to fit the problem into nodes with less system memory. The high memory requirements can be overcome by simple dividing the normal equations into multiple sections and computing each block sequence one after the other. The upper bound of memory demand can then be set to appropriate values to comply with the given hardware situation. The basic principle is outlined in figure 6.3.

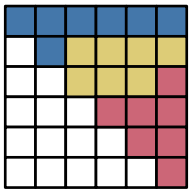

Figure 6.3: Schematic principle of the reduction of the memory requirement for the assembly of the normal equations by dividing the computations into multiple turns. The algorithm for the computation of the temporal normal equations is then performed for each block subset.

While the number of floating point operations remains constant for any number of turns, a parallel overhead may occur since, for each turn an additional possible idle point is introduced, which can be observed in algorithm 6.3.
In the distribution step, the dependencies between the individual normal equation blocks and processes are resolved. This means that for each normal equation block all processes which require said block for further computations are determined. The block is then broadcast within the subset. Figure 6.4 shows the occurrence of the first static normal equation block for the interval $\mathcal{I}_1$.

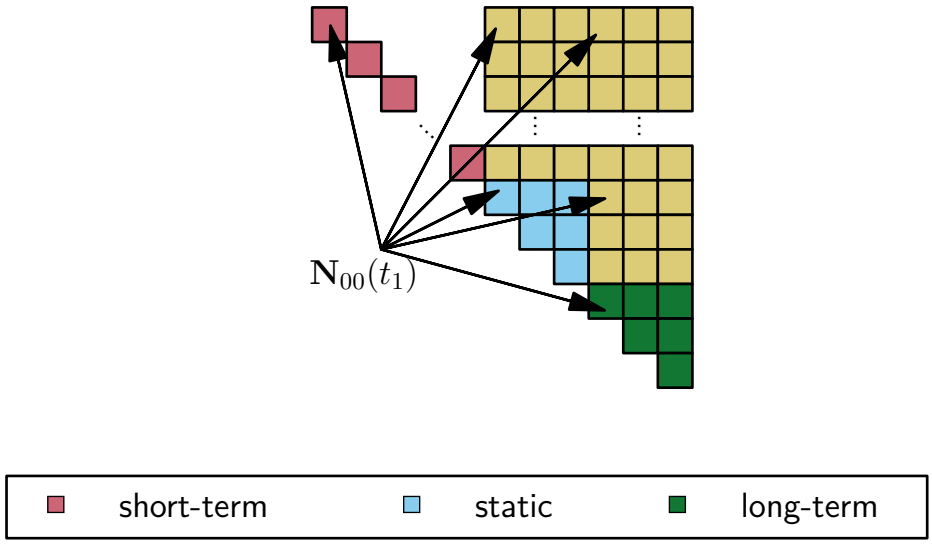

Figure 6.4: Normal equation blocks which depend on the static normal equation block $\mathbf{N}_{00}(t_1)$. $\mathbf{N}_{00}(t_1)$ is broadcast within the process subset which hold these blocks according to the present blockcyclic distribution. This example shows the upper triangle of the normal equation matrix with modeled daily variations and a single long-term gravity field variation.

After the broadcast of the normal equation block, each process applies the temporal factors $\Phi^{(k)}\Phi^{(l)}$ and accumulates the block. The distribution step is performed for each normal equation block $\mathbf{N}_{\alpha\beta}$ and each interval $\mathcal{I}_i$.
The last step in the normal equation assembly is the integration of the short term regularization matrices described in section 6.1.1. This is done by forming the normal equation matrix for the pseudo observations and adding the resulting diagonal and off diagonal blocks to the previously assembled short-term normal equations.

6.2.3 Elimination of Epoch-dependent Parameters

In the last step of the algorithm the parameter groups modeled for a certain time span, namely short-term variations and satellite specific parameters are eliminated to allow accumulation of the normal equations for the parameters corresponding to the static gravity field and long-term variations. The elimination is performed on a normal-equation basis as outlined in section 5.3. Equation (5.20) can also be interpreted as an incomplete Cholesky decomposition performed on the full normal equations. To emphasize this equivalence, a form of the recursive blocked Cholesky decomposition algorithm (for example Choi et al., 1994) shall be outlined. The key statement of the Cholesky decomposition is that every symmetric and positive definite matrix can be expressed via an upper or lower triangular matrix (e.g. Higham, 2002). Applied to the subdivided normal equations this means that the block matrix in (5.18) can be decomposed into the matrix product

$$\begin{bmatrix} \mathbf{N}_{11} & \mathbf{N}_{12} \\ \mathbf{N}_{12}^T & \mathbf{N}_{22} \end{bmatrix} = \begin{bmatrix} \mathbf{R}_{11}^T & 0 \\ \mathbf{R}_{12}^T & \mathbf{R}_{22}^T \end{bmatrix} \begin{bmatrix} \mathbf{R}_{11} & \mathbf{R}_{12} \\ 0 & \mathbf{R}_{22} \end{bmatrix}. \tag{6.13}$$

Performing the matrix multiplication in (6.13) leads to the expressions for each block of the

normal equations

$$\begin{aligned}\mathbf{N}_{11} &= \mathbf{R}_{11}^T\mathbf{R}_{11}\\ \mathbf{N}_{12} &= \mathbf{R}_{11}^T\mathbf{R}_{12}\\ \mathbf{N}_{22} &= \mathbf{R}_{12}^T\mathbf{R}_{12} + \mathbf{R}_{22}^T\mathbf{R}_{22}.\end{aligned} \tag{6.14}$$

Substituting the first two expression in (6.14) into (5.19) leads to the reduced normal equation system in $\mathbf{x}$ where

$$\bar{\mathbf{N}} = \mathbf{N}_{22} - \mathbf{R}_{12}^T\mathbf{R}_{12} \quad \text{and} \quad \bar{\mathbf{n}} = \mathbf{n}_2 - \mathbf{R}_{12}^T\mathbf{R}_{11}^{-T}\mathbf{n}_1. \tag{6.15}$$

Formulating the parameter elimination based on normal equations in algorithmic form leads to algorithm 6.2.

Algorithm 6.2: Parameter elimination based on normal equations via incomplete Cholesky decomposition. In practice, the elimination is performed in-place which means the corresponding blocks of the normal equation matrix are overwritten during the decomposition process.

Input:
$\begin{bmatrix}\mathbf{N}_{11} & \mathbf{N}_{12}\\ \mathbf{N}_{12}^T & \mathbf{N}_{22}\end{bmatrix}, \begin{bmatrix}\mathbf{n}_1\\ \mathbf{n}_2\end{bmatrix}$ ... full normal equation system in blocked form

Output:
$\bar{\mathbf{N}}, \bar{\mathbf{n}}$ ... reduced normal equation system

---

(1) Cholesky decomposition of diagonal block $\mathbf{N}_{11}$

$$\mathbf{N}_{11} \rightarrow \mathbf{R}_{11}$$

(2) Backward substitution of off-diagonal block (and right-hand-side)

$$\mathbf{R}_{12} \leftarrow \mathbf{R}_{11}^{-T}\mathbf{N}_{12}, \qquad \mathbf{n}_1^* \leftarrow \mathbf{R}_{11}^{-T}\mathbf{n}_1$$

(3) Update of leading diagonal block (and right-hand-side)

$$\mathbf{N}_{22} \leftarrow \mathbf{N}_{22} - \mathbf{R}_{12}^T\mathbf{R}_{12}, \qquad \mathbf{n}_2 \leftarrow \mathbf{R}_{12}^T\mathbf{n}_1^*$$

Since the parameter groups daily and satellite have to be eliminated before accumulating the monthly normal equations, some precautions concerning the memory evolution during the incomplete Cholesky algorithm have to be taken. Ideally, the parameter order is chosen in such a way, that no fill-elements occur during the update step in the Cholesky algorithm and the sparsity structure of the normal equation matrix is preserved.
For the problem at hand this means that due to the correlation structure of the modeled short-term variations the only sensible parameter order is *short-term*, *satellite*, *static* and *long-term* as presented in figure 6.1. This leads to a so called *kite-structure* (e.g. Schuh, 1996 or Boxhammer, 2006) of the normal equation matrix which preserves the matrix structure during the application of the Cholesky decomposition.

6.3 Detailed Algorithm

In the following section, the algorithmic implementation of the steps previously described will be presented. As a first step, the notation used in the assembly of the temporal normals shall be described in detail. For convenience sake the parameter group *satellite* is included as first entries of the static gravity field parameter vector.
The full normal equation matrix containing short- and long term temporal variations as well as the static part is denoted as $\mathbf{N}$ without any sub- or superscripts. A single sub-block is indicated with greek letter subscripts e.g. $\mathbf{N}_{\alpha\beta}$. The normal equation matrix for a single interval $\mathcal{I}_i$ is denoted as $\mathbf{N}(t_i)$. The total number of arcs is described by n_{arcs}, the number of intervals by N and the number of temporal factors n_Φ. For-loops are described in MATLAB notation which means the domain of the control variable j in $j = 0 : n_{\text{arcs}} - 1$ is $\{0, 1, \ldots, n_{\text{arcs}} - 1\}$.
The normal equation matrix is assumed to be distributed blockcyclicly as indicated in Figure 6.2. The number of blocks per parameter group is evidently dictated by the number of parameters modeled. In the following these block counts are denoted with $b_{\text{short-term}}$ (for a single interval), b_{static} and $b_{\text{long-term}}$ (for a single temporal factor $\Phi_i^{(k)}$) respectively.

Table 6.2: Total number of blocks for each parameter group.

parameter group	block count
short-term	$N \cdot b_{\text{short-term}}$
static	b_{static}
long-term	$n_\Phi \cdot b_{\text{long-term}}$

The starting block for each parameter group within the normal equation matrix can be derived by taking the cumulative sum of the expressions in table 6.2. Algorithm 6.3 describes the computation of the observation equations and interval-wise normal equations blocks, while algorithm 6.4 deals with the distribution of the blocks and the accumulation of the temporal normal equations.

Algorithm 6.3: Parallel assembly of the static normal equation system. Only the block of the upper triangle of the static normal equation matrix are computed and kept in memory.

Input:
Processed L1B-data for the computation of $\mathbf{A}$ and $\mathbf{l}$

Output:
$\mathbf{N}_{\alpha\beta}(t_i), \mathbf{n}_\beta(t_i) \ldots$ interval-wise static normal equations

for $j = 0 : n_{arcs} - 1$**:**
  `/* loop scheduled according to algorithm 6.1 */`
  compute observation equation $\mathbf{A}_j$ and observation vector $\mathbf{l}_j$
for $j = 0 : n_{arcs} - 1$**:**
  compute static normal equations $\mathbf{N}(t_i)$
  if $j \in \mathcal{I}_i$**:**
    $\mathbf{N}(t_i) \leftarrow \mathbf{N}(t_i) + \mathbf{A}_j^T \mathbf{A}_j$

Algorithm 6.4: Computation of the full normal equation system consisting of short-term, long-term and static parameter groups, based on the normal equations for each interval.

Input:
$\Phi_i^{(k)}$ ... temporal representations of the long-term variations
$\mathbf{B}, \mathbf{Q}$ ... a-priori information for regularization of short-term variations
$\mathbf{N}_{\alpha\beta}(t_i), \mathbf{n}_\beta(t_i)$ ... interval-wise static normal equations

Output:
$\bar{\mathbf{N}}, \bar{\mathbf{n}}$ ... reduced normal equation system for static field and long-term variations

---

for $i = 0 : n_I - 1$**:**
  for *all blocks* $\mathbf{N}_{\alpha\beta}(t_i)$**:**
    reduce (summation) $\mathbf{N}_{\alpha\beta}(t_i)$ on a single process p
    determine process subset $\mathcal{P}$ which requires $\mathbf{N}_{\alpha\beta}(t_i)$
    broadcast $\mathbf{N}_{\alpha\beta}(t_i)$ within $\mathcal{P}$ with root p

    `/* short-term variations */`
    if $\alpha, \beta < b_{\text{short-term}}$**:**
      $(\gamma, \delta) \leftarrow (i, i)$
      $\mathbf{N}_{\gamma\delta} \leftarrow \mathbf{N}_{\alpha\beta}(t_i)$

    `/* short-term variations ↔ static field */`
    if $\alpha < b_{\text{short-term}}$**:**
      $(\gamma, \delta) \leftarrow (i, N \cdot b_{\text{short-term}} + \beta)$
      $\mathbf{N}_{\gamma\delta} \leftarrow \mathbf{N}_{\alpha\beta}(t_i)$

    `/* short-term variations ↔ long-term variations */`
    if $\alpha < b_{\text{short-term}} \wedge \beta < b_{\text{long-term}}$**:**
      for $k = 0 : n_\Phi - 1$**:**
        $(\gamma, \delta) \leftarrow (i, N \cdot b_{\text{short-term}} + k \cdot b_{\text{long-term}} + \beta)$
        $\mathbf{N}_{\gamma\delta} \leftarrow \Phi_i^{(k)} \mathbf{N}_{\alpha\beta}(t_i)$

    `/* static gravity field parameters */`
    $(\gamma, \delta) \leftarrow N \cdot b_{\text{short-term}} + (\alpha, \beta)$
    $\mathbf{N}_{\gamma\delta} \leftarrow \mathbf{N}_{\gamma\delta} + \mathbf{N}_{\alpha\beta}(t_i)$

    `/* static-gravity field ↔ long-term variations */`
    if $\beta < b_{\text{long-term}}$**:**
      for $k = 0 : n_\Phi - 1$**:**
        $(\gamma, \delta) \leftarrow N \cdot b_{\text{short-term}} + (\alpha, k \cdot b_{\text{long-term}} + \beta)$
        $\mathbf{N}_{\gamma\delta} \leftarrow \mathbf{N}_{\gamma\delta} + \Phi_i^{(k)} \mathbf{N}_{\alpha\beta}(t_i)$

    `/* long-term variations */`
    if $\alpha, \beta < b_{\text{long-term}}$**:**
      for $k = 0 : n_\Phi - 1$**:**
        for $l = k : n_\Phi - 1$**:**
          $(\gamma, \delta) \leftarrow N \cdot b_{\text{short-term}} + b_{\text{static}} + (k \cdot b_{\text{long-term}} + \alpha, l \cdot b_{\text{long-term}} + \beta)$
          $\mathbf{N}_{\gamma\delta} \leftarrow \mathbf{N}_{\gamma\delta} + \Phi_i^{(k)} \Phi_i^{(l)} \mathbf{N}_{\alpha\beta}(t_i)$

compute normal equations $\mathbf{R}$ for the pseudo observations from $\mathbf{B}$ and $\mathbf{Q}$
$\mathbf{N} \leftarrow \mathbf{N} + \mathbf{R}$
apply incomplete Cholesky decomposition (algorithm 6.2) to obtain $\bar{\mathbf{N}}, \bar{\mathbf{n}}$

7 Gravity Field Recovery

The following chapter gives an overview of the functional model and used input data as well as the background models used in the gravity field recovery process.

7.1 Observation Model

The observation equations used in the real data analysis were set up as outlined in section 4 for both KBR and POD observables. The arc length was chosen with 90 minutes which corresponds to about one revolution of the satellite pair.
In addition to the unknown gravity field parameters, the boundary positions for each arc as well as accelerometer calibration parameters were estimated. These parameters were eliminated beforehand to allow the accumulation of the monthly normal equations for the whole time series.
For each satellite a constant accelerometer bias was estimated per arc as well as a scale factor for each month.

7.2 Input Data, Background Models and Processing Strategy

7.2.1 Input Data

As already mentioned in the beginning of this section, GRACE data in the time span of 2004-01 to 2012-12 was used to compute various gravity field solutions to determine the effect of the combined estimation of static and time variable gravity field. The primary observables used in this process are K-band range rates and kinematic orbits in form of POD positions (Zehentner and Mayer-Gürr, 2013) with corresponding 3×3 covariance matrix for both GRACE-A and GRACE-B. Furthermore, the non-conservative forces were reduced using the accelerometer data provided for both satellites. These acceleration time series were corrected using the bias and scale factors suggested in Bettadpur, 2009 and their sampling is reduced to 5 s to match the KBR measurements. A detailed overview of the used data sets for the gravity field recovery can be found in table 7.1.

Table 7.1: GRACE-L1B data used in the gravity field recovery process.

Data Set	
K-band range-rate	5 s sampling rate
light-time correction	5 s sampling rate
KBR antenna center variations	5 s sampling rate
POD positions	300 s sampling rate
Star Camera Assembly quaternions	5 s sampling rate
Accelerometer measurements	5 s sampling rate

7.2.2 Background Models

When performing gravity field recovery from satellite data, all other forces acting on the satellite have to be reduced beforehand. These disturbing forces are either measured by the on board accelerometer or described via appropriate models. A short summary of the models reduced from the GRACE-L1B data is given in table 7.2.

Table 7.2: Background models used in the gravity field recovery process.

Effect	Model
Third body forces	JPL DE405 (Standish, 1998) ephemerides
Solid Earth Tides, Pole Tides	IERS Conventions 2003 (McCarthy and G., 2004)
Ocean Tides	EOT11a model (Savcenko and Bosch, 2011)
Ocean Pole Tides	according to Desai, 2002
Atmospheric Tides	Biancale and Bode, 2006
De-aliasing	AOD1B (Flechtner et al., 2014)
Long-term temporal variations	ITG-Grace2010 (Mayer-Gürr et al., 2010b)
Relativistic corrections	IERS Conventions 2003 (McCarthy and G., 2004)

As a static reference model, the ITG-Grace2010s GRACE-only solution was used.

7.2.3 Regularization of Daily Solutions

As mentioned in 3.2 the daily solutions have to be regularized in order to obtain reliable estimates.
In the study at hand the spatial and temporal correlations of the short-term variations were derived using a time series of 25 years of geophysical models in the time span of 1976 to 2000 in analogy to Kurtenbach, 2011. The derived covariance matrices shall describe the properties of residual ocean and atmospheric signal as well as unmodelled mass variations such as continental hydrology.
Concerning ocean and atmospheric variations it is assumed that after the dealiasing process by application of the AOD1B product only residual signal not modeled in the de-aliasing product is remaining. Since no uncertainty information for the individual AOD1B components is available, the distribution in magnitude of this residual signal is modeled via the magnitude of the complete signal of the respective components. This means that in regions with larger signal amplitudes, larger errors are expected and more variability of the short-term gravity parameters is allowed.
Furthermore an isotropic noise content is added to the spatial covariance matrix as is proposed in Kurtenbach, 2011 to also account for errors in regions with little temporal variability. Table 7.3 describes the geophysical models used to derive the coveriance matrices and their respective scaling.

Table 7.3: Geophysical model used to derive the state-transition matrix **B** and their respective scaling.

Process	Model	Amplitude Scale
Ocean	OMCT (Dobslaw and Thomas, 2007)	0.5
Atmosphere	ECMWF (ECMWF Research Department, 2013)	0.5
Hydrology	WGHM (Döll et al., 2003)	1.0

As can be seen the residual signals in both ocean and atmosphere are assumed to have 50% of the total signal which was chosen in accordance to Kurtenbach, 2011. Since continental hydrology is not included in the AOD1B product, the full signal is used as error budget. The temporal variability of the resulting process is shown in figure 7.1. It shows the RMS for each grid point in time for the period 1976-2000 used to derive the empirical covariance matrices.

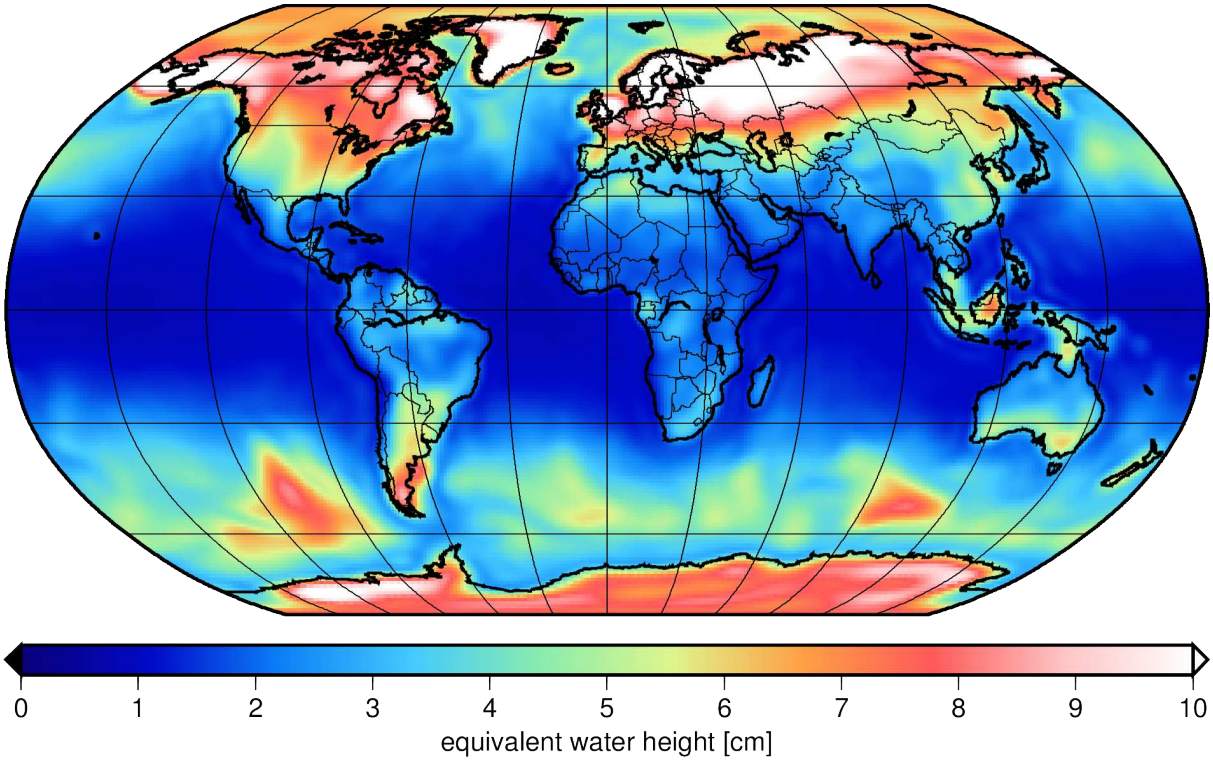

Figure 7.1: Temporal variability of the expected residual signal in equivalent water height. RMS: 3.96 cm, Min: 0.73 cm, 14.50 cm.

7.2.4 Regularization of Long-term Temporal Variations

In addition to the short-term temporal variations, the modeled secular and annual variations were regularized as well. This was done using a Kaula-like function (Kaula, 1966) adapted to the trend and annual signal. The curves were derived from secular and annual variations estimated from monthly solutions provided by CSR (Bettadpur, 2012) by tailoring the power β of the degree variances

$$\sigma_n^2 = \alpha \frac{1}{n^\beta}. \tag{7.1}$$

The variable scale factor α was included for convenience reasons only, since it is later adjusted with the respective variance component as can be seen in (5.21). For the annual variation, a single set of degree variances was used in the regularization process, however individual regularization parameters were modeled for sine and cosine coefficients in the variance component estimation.
The obtained curves with the respective signals are shown in figure 7.2.

7.2.5 Processing Strategy

The gravity field recovery process for each of the computed solutions was split into three major processing steps which will be discussed in this section.

Data preparation In the first step the GRACE-L1B data is re-sampled to the sampling rates listed in table 7.1 if necessary and divided into arcs with a maximum length of 90 minutes. If a data gap is encountered, the previous epoch is set as last within the

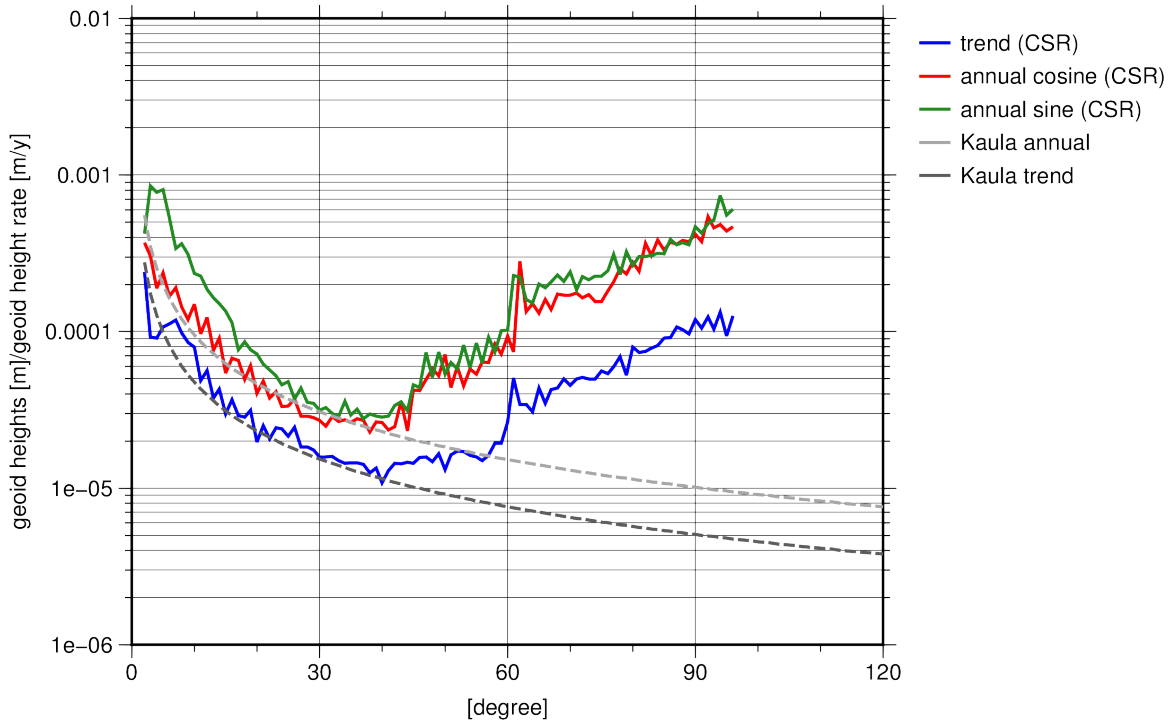

Figure 7.2: Isotropic regularization curves used for the stabilization of the long term temporal variations. The annual and trend signals have been estimated from CSR monthly solutions (Bettadpur, 2012).

current arc and a new arc is set up. This means the individual arcs do no contain any data gaps and possess as a constant sampling of 5 s. The lower bound for the arc length was chosen with 30 minutes to reduce the number of boundary values to be estimated.

The resulting arc sequences for each data set are then stored in monthly groups for further processing.

Normal equation formation For each monthly data set, a temporal covariance function was estimated for both K-band observables and POD positions. Furthermore individual weighting factors for each arc were derived for each observation group. These two steps were performed using the iterative procedure described in Mayer-Gürr, 2013. The functional model used in this step was composed of a low degree static field (up to degree and order 60) as well as daily gravity field variations up to degree and order 40 with a-priori information as described in section 7.2.3. The accelerometer scale factor and bias was modeled according to the observational model described in section 7.1.

After determination of the stochastic model, the full normal equations with the parametrizations outlined in table 7.4 were assembled using the algorithm presented in section 6.3.

Solution of the Normal Equations The monthly normal equations assembled in the previous step were accumulated in a first step within each year and then, in a second step to form the full normal equations for the whole investigation period.

For solutions consisting of multiple temporal variations, an individual variance component was set up for each temporal constituent (e.g., secular, annual cosine and annual sine) to estimate the corresponding regularization parameter (see also section 7.2.4).

The solution was computed based on the Cholesky decomposition of the normal equation

matrix by forward-/backward substitution (Higham, 2002).

The reference models as well as the mean of the AOD1B product were added back to the computed solution vectors which means that each obtained solution includes the complete gravity field signal including ocean and atmosphere.

The work flow and dependencies of the individual processing step is depicted in figure 7.3.

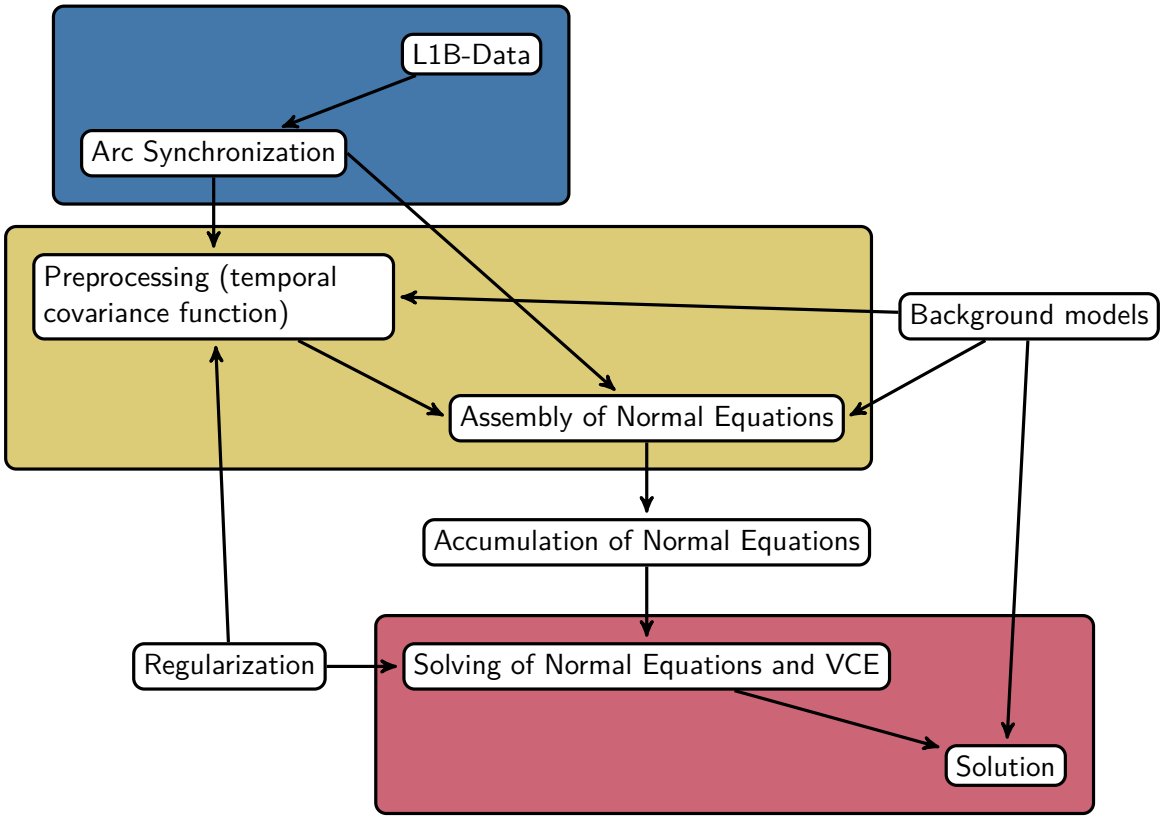

Figure 7.3: Schematic work flow of the gravity field recovery process. The complete processing of the GRACE data was split into three major work packages: data preparation (blue), normal equation assembly (ocher) and solution of the normal equations (red).

7.3 Gravity Field Solutions

To evaluate the impact of the combined estimation of short- and long-term variations as well as the static gravity field component, three gravity field solutions were computed using the same L1B input data and accelerometer model. The parametrization of the individual solutions was chosen to investigate different effects in the combination of static and temporal variations. As a baseline, a straightforward static-only parametrization of the gravity field was computed. The resulting solution is denoted *static-only* in the following. To investigate the incorporation of daily variations, a second set of normal equations with modeled daily gravity field variations (*short-term-only* solution) according to section 6.1.1 was computed. In a last step, a *combined* solution with modeled short- and long-term variations was computed to the impact of incorporating multiple time scales into the gravity field recovery process.
Table 7.4 gives an overview of the used gravity field parametrizations and spherical harmonic representations.

Table 7.4: Gravity field parametrizations of the computed solutions and respective spherical harmonic representations in degree/order (d/o).

	short-term	long-term	static
static-only	-	-	d/o 2 to 200
short-term-only	d/o 2 to 40	-	d/o 2 to 200
combined solution	d/o 2 to 40	trend, annual: d/o 2 to 120	d/o 2 to 200

The obtained solutions were compared to the independent GOCE (Gravity Field and Steady-State Ocean Circulation Explorer) time-wise approach model TIM05 (Brockmann et al., 2014). Due to the fact that GRACE provides higher sensitivity to the long wavelength part of the gravity field than GOCE, comparison of lower spherical harmonic degrees proves to be difficult. Since no independent data sets are available due to data and/or processing overlap, the comparison with GRACE gravity fields is omitted.

7.3.1 Comparison of Static Solutions

When comparing gravity fields in spectral domain, a popular method of visualization are degree variances or degree amplitudes σ_n (Mayer-Gürr, 2006). In principle they represent the degree wise coefficient differences to a reference field in terms of an error RMS. These can be approximately scaled to geoid heights by multiplying the degree wise coefficient difference square sum with the Earth's radius R

$$\sigma_n = R\sqrt{\sum_{m=0}^{n}[(c_{nm} - c_{nm}^{\text{ref}})^2 + (s_{nm} - s_{nm}^{\text{ref}})^2]}. \tag{7.2}$$

Due to GOCE's sun-synchronous orbit, no observations are taken in the polar regions which means that the gravity field suffers in these areas (Metzler and Pail, 2005). In the spectral domain this means that the zonal and near-zonal coefficients cannot be determined very accurately by this satellite. The maximum order affected by this polar gap can be determined by the rule of thumb proposed in Gelderen and Koop, 1997,

$$m_{\max} \approx |\frac{\pi}{2} - I| \cdot n, \tag{7.3}$$

where I denotes the satellite's inclination. The aperture angle α_A of the polar cap is tied to the inclination I of the satellite by $\alpha_A = |0.5\pi - I|$. In this thesis an aperture angle of 8 degrees is used in comparisons with GOCE only gravity field models, which completely covers the polar gap (GOCE's inclination is approximately 96.5 degrees, c.f. Drinkwater et al., 2007).
A direct comparison of spherical harmonic coefficients can be performed by using coefficient triangles which sort the individual coefficients degree- and order-wise.
Furthermore, the gravity field solutions are compared in space domain by means of geoid heights.
Figure 7.4 shows the error degree amplitudes with respect to the GOCE-only model TIM05.
As can be seen, the incorporation of short term variations improves the static solution significantly, starting at degree 40. Similarly the modeled long-term variations improve the solution in the short wavelength part of the gravity field, even past the maximum degree of 120. Both these effects support the fact that unmodeled temporal variations, impact the static gravity field estimates in frequency bands where no time variable signal is expected.

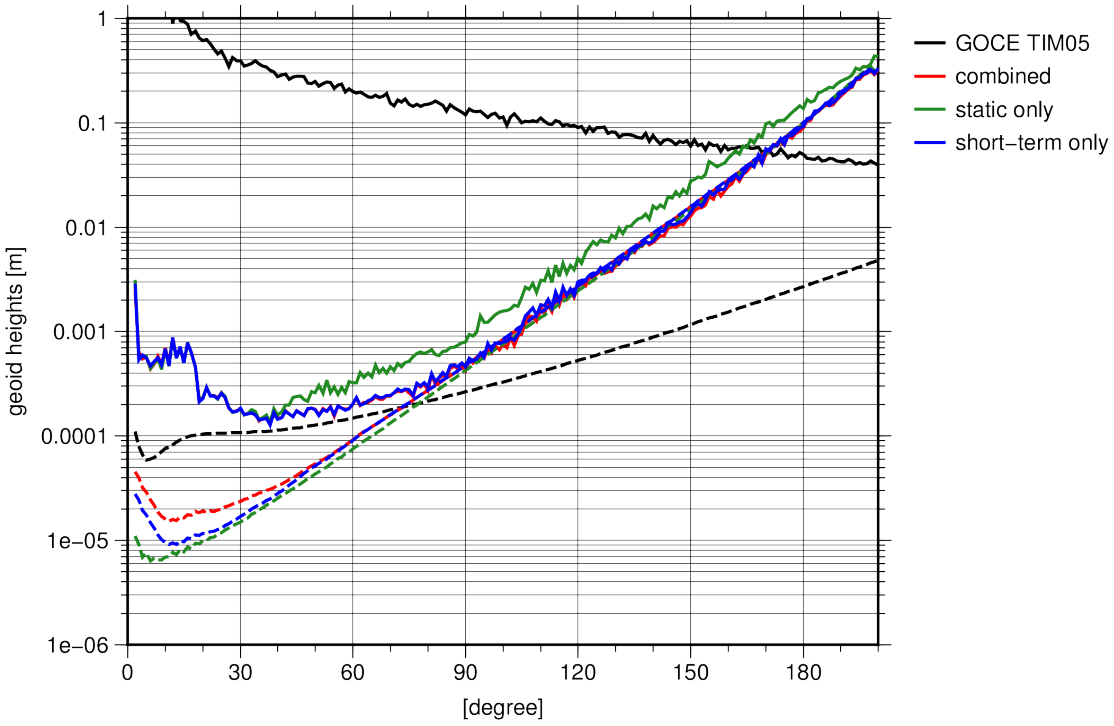

Figure 7.4: Degree error variances with respect to the GOCE-only model GOCE-TIM05. The dashed lines represent the formal errors of the respective gravity field solutions. A polar gap with an aperture angle of 8 degrees was used.

A similar picture occurs when comparing the different solution in the spatial domain. The static-only solution exhibits globally distributed striping patterns (see figure 7.5), while these effects are greatly reduced in the combined solution. This is also reflected in the geoid height RMS which is reduced from approximately 6.4 cm to 3.8 cm.
When examining the individual coefficient differences in figure 7.7 large errors in the GRACE resonant orders (15 and multiples thereof, see for example Seo et al., 2008) occur. These order-wise effects are drastically reduced when incorporating the daily gravity field variations in the estimation of the long-term mean field (see figure 7.8).
Figures 7.9a and 7.9b show the formal errors for each estimated coefficient for the static-only and combined solution respectively. Apart from the fact that the formal errors of the static solution are lower, which is explained through the different number of estimated parameters, distinctive stripes can be seen in the resonance orders for the combined solution.
Since observational model and satellite specific parametrization is identical for both solutions, these increased formal errors are attributed to the additional modeling of short-term variations in the combined solution. This circumstance can be seen as an improvement of the stochastic model for the spherical harmonic coefficients, since larger errors in these orderwise bands are expected (Meyer et al., 2012).

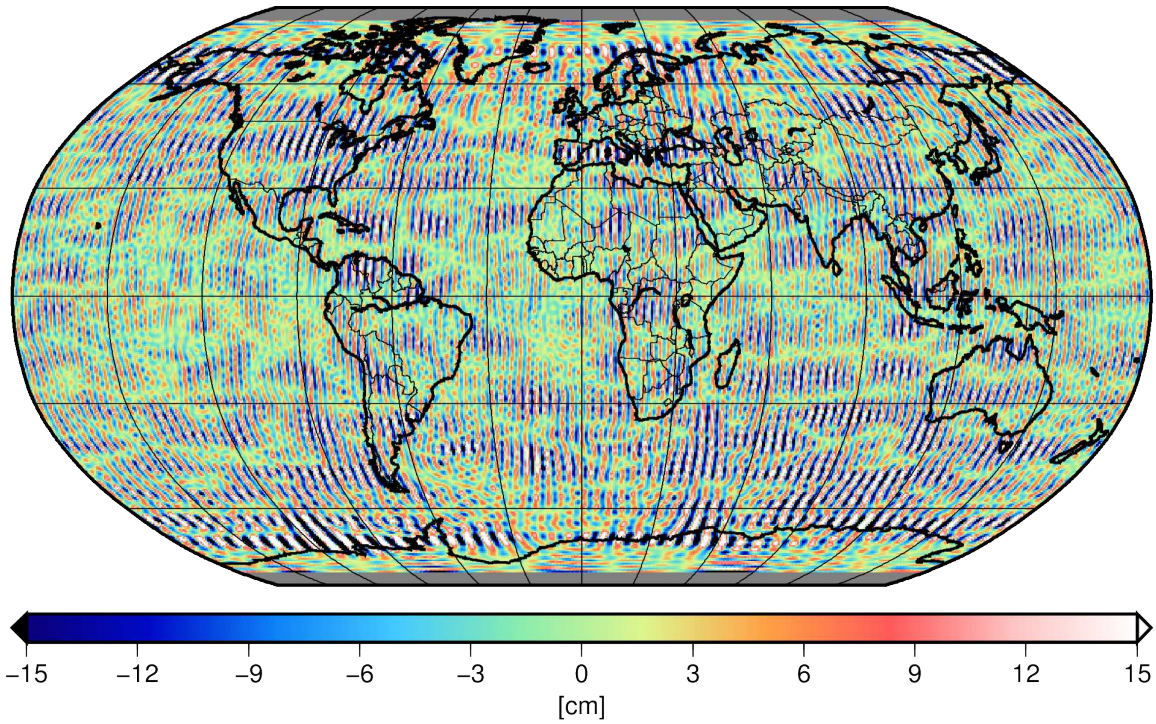

Figure 7.5: Differences between GOCE TIM05 and the static-only solution (up to degree and order 150) in geoid heights. RMS: 6.39 cm, Min: -67.19 cm, Max: 66.75 cm.

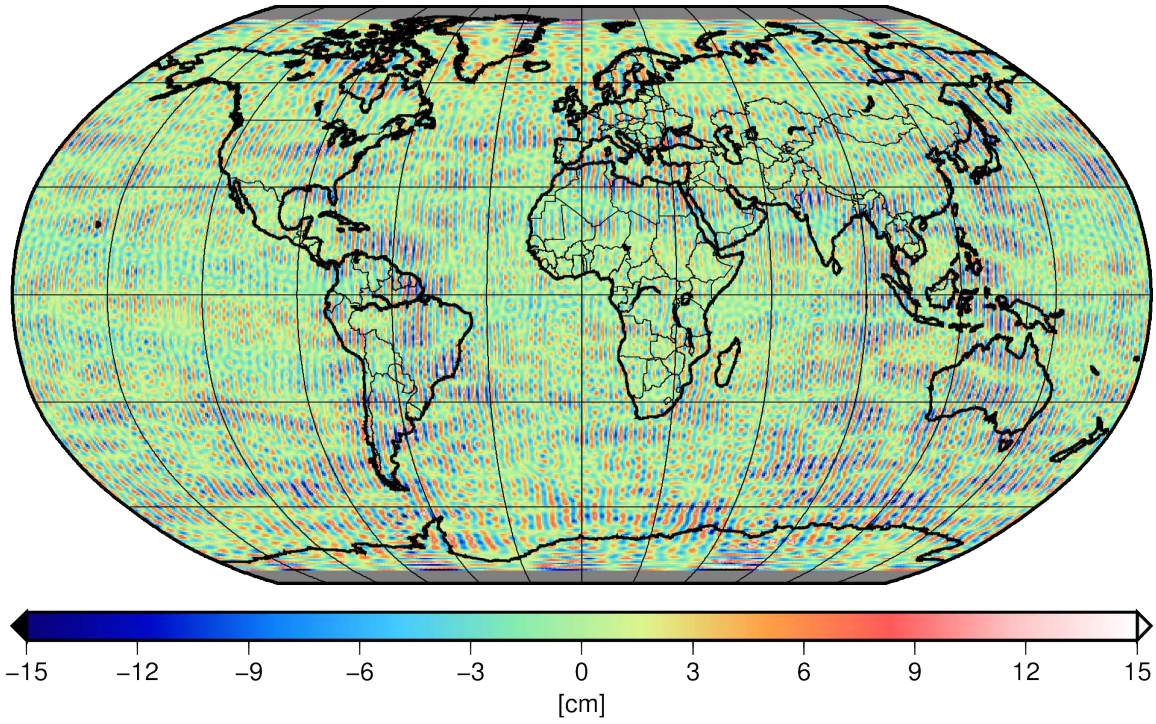

Figure 7.6: Differences between GOCE TIM05 and the combined solution (up to degree and order 150) in geoid heights. RMS: 3.77 cm, Min: -25.18 cm, Max: 17.28 cm.

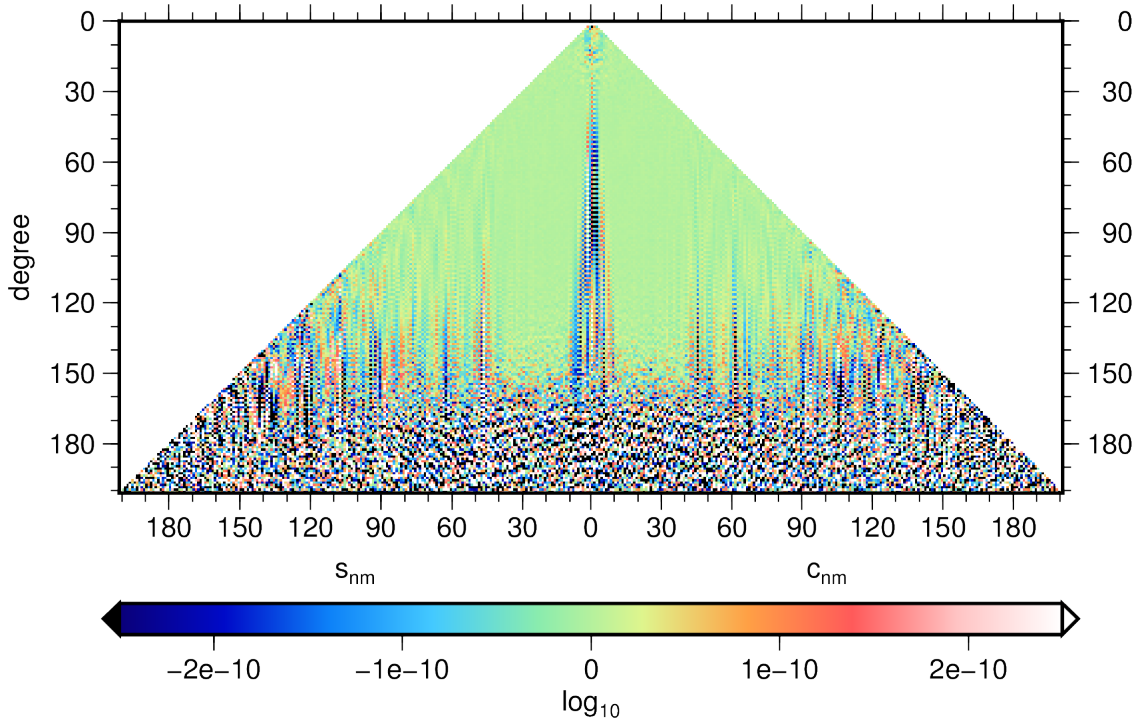

Figure 7.7: Coefficient differences between GOCE TIM05 and the static-only solution.

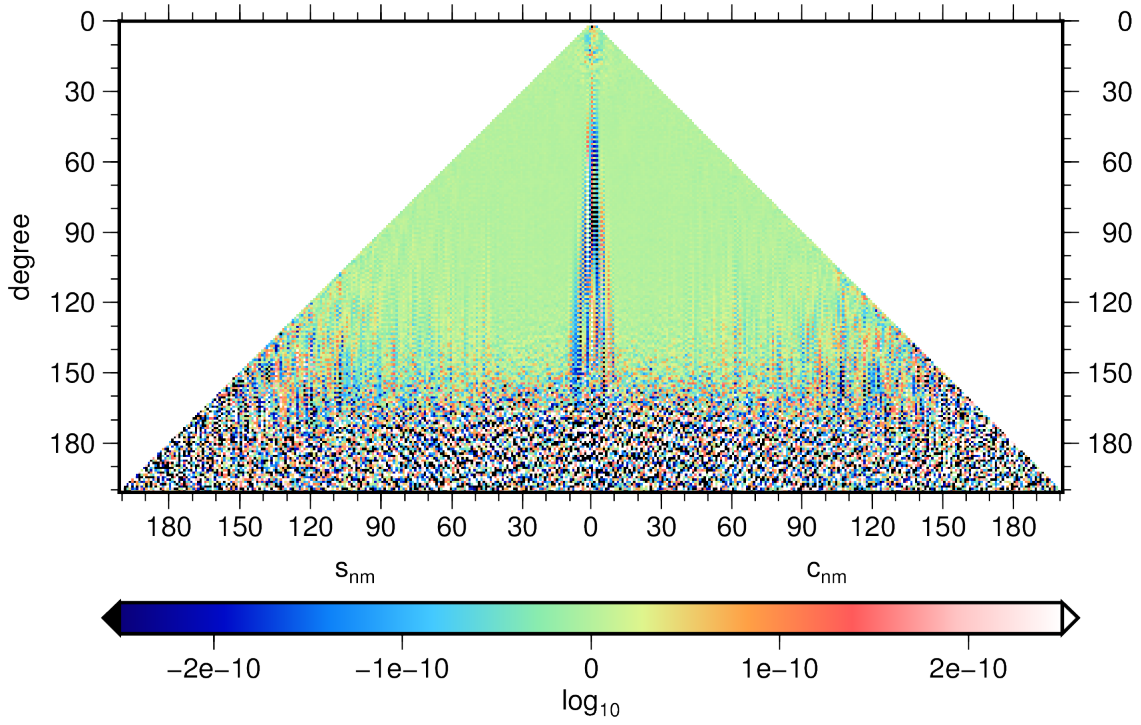

Figure 7.8: Coefficient differences between GOCE TIM05 and the combined solution.

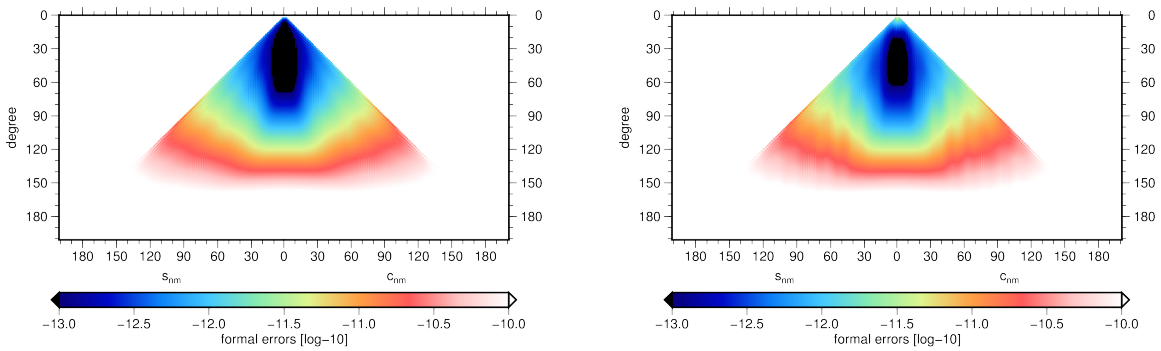

(a) Static-only solution.

(b) Combined solution.

Figure 7.9: Formal errors of the static and combined solutions.

7.3.2 Estimated Long-term temporal Variations

In the combined solution, spherical harmonic coefficients for secular and annual temporal variations were obtained in addition to the static solution. Since a-priori information was introduced into the adjustment process, the respective contribution of GRACE and regularization has to be reviewed. The contribution of GRACE to the solution vector can be seen as measure of how much time variable signal the mission can extract using the data at hand.
As can be seen in figures 7.10, 7.11 and 7.12, the grace observations contribute to the obtained solutions approximately up to degree 80 (annual oscillation) and up to degree 100 (secular variation). However, a strict truncation of the expansion at the bounds mentioned prior neglects the fact that the spherical harmonic representation constitutes a global mean. This means that signal in regions with high temporal variability such as Greenland is possibly lost.
Figure 7.13 shows the estimated secular variations in terms of equivalent water height. High change rates can be observed in regions with postglacial rebound (Canada, Finnoskandia) as well as active cryosphere (Greenland, Antarctica, see also figure 7.14).
The effect of large earthquakes is clearly visible, specifically off the coast of Chile (February 2010, U.S. Geological Survey, 2014), Japan (March 2011, U.S. Geological Survey, 2014) and Sumatra (December 2004, Park et al., 2005). These gravity signals are not of continuous nature and a parametrization as linear trend is not appropriate. Therefore an additional piecewise representation taking such events into account is suggested.
Figures 7.15 and 7.16 show the estimated cosine and sine coefficients for the annual oscillation respectively. As is clearly visible, the main signal part of this temporal variation is primarily confined to the continents. This is expected since the full hydrological signal is still present in the GRACE-L1B data as explained in section 7.2.3.

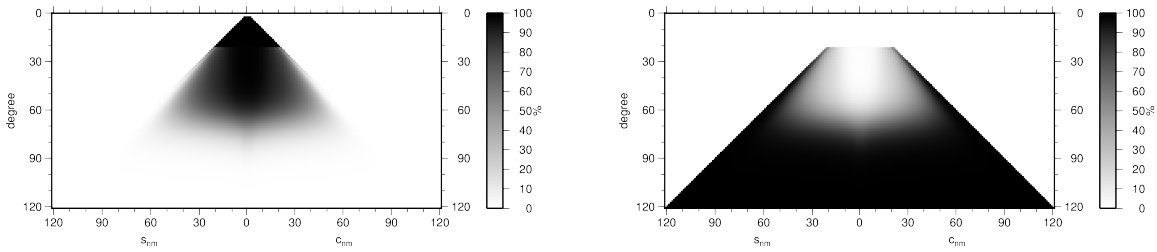

(a) GRACE. (b) Regularization.

Figure 7.10: Individual contributions of GRACE and a-priori information to the estimated annual oscillation (cosine coefficients) in percent.

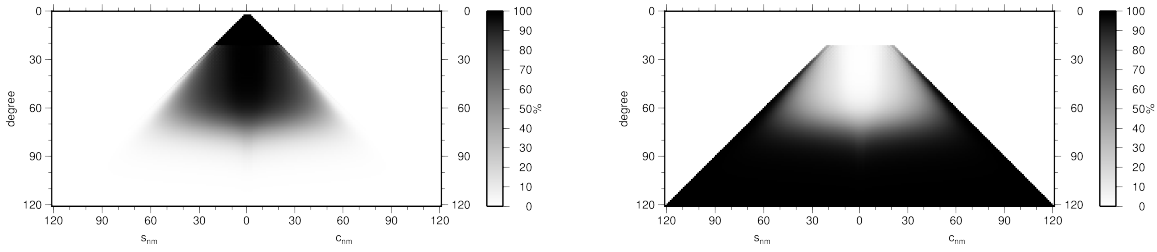

(a) GRACE. (b) Regularization.

Figure 7.11: Individual contributions of GRACE and a-priori information to the estimated annual oscillation (sine coefficients) in percent.

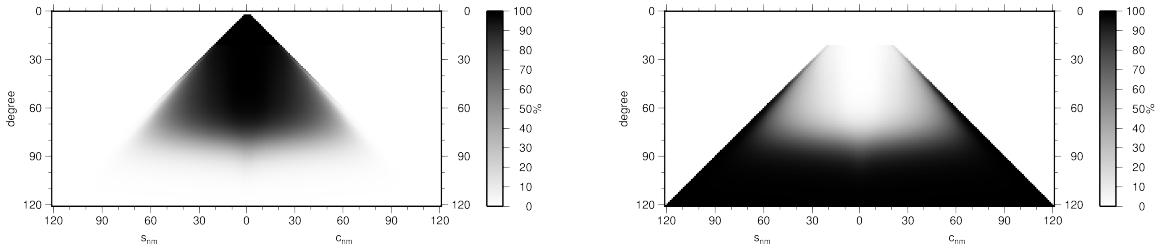

(a) GRACE. (b) Regularization.

Figure 7.12: Individual contributions of GRACE and a-priori information to the estimated secular gravity field variations in percent.

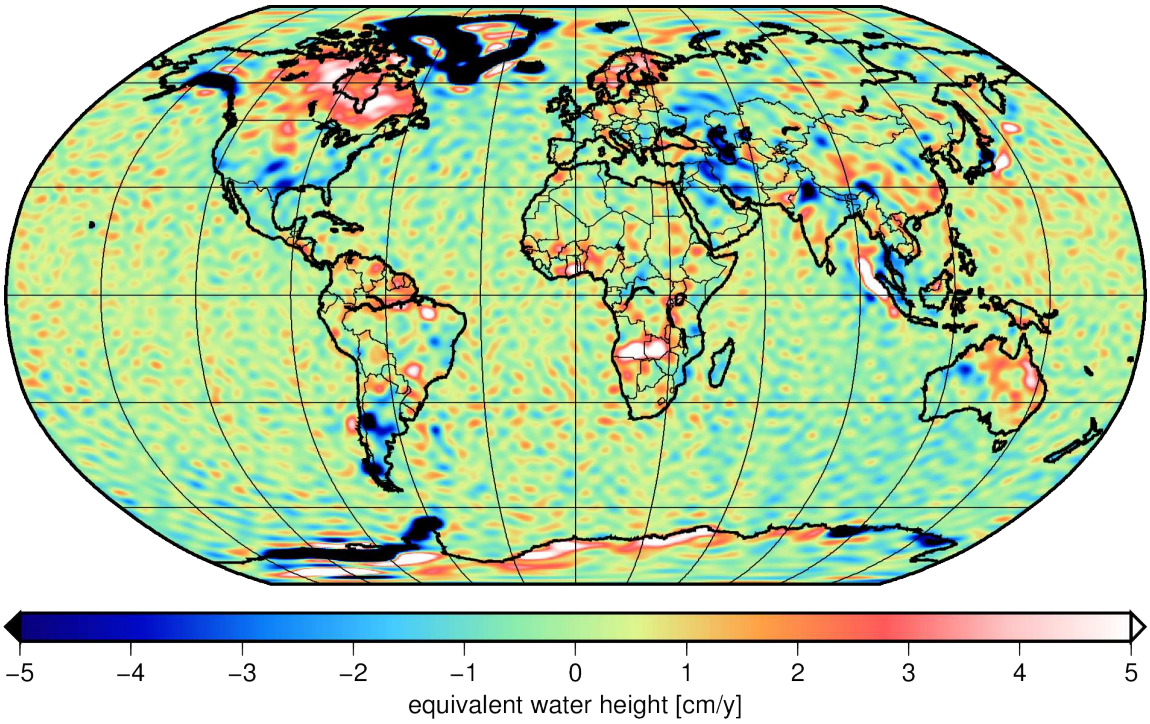

Figure 7.13: Estimated secular temporal variations in terms of equivalent water height per year. Min: -57.65 cm/y, Max: 21.89 cm/y.

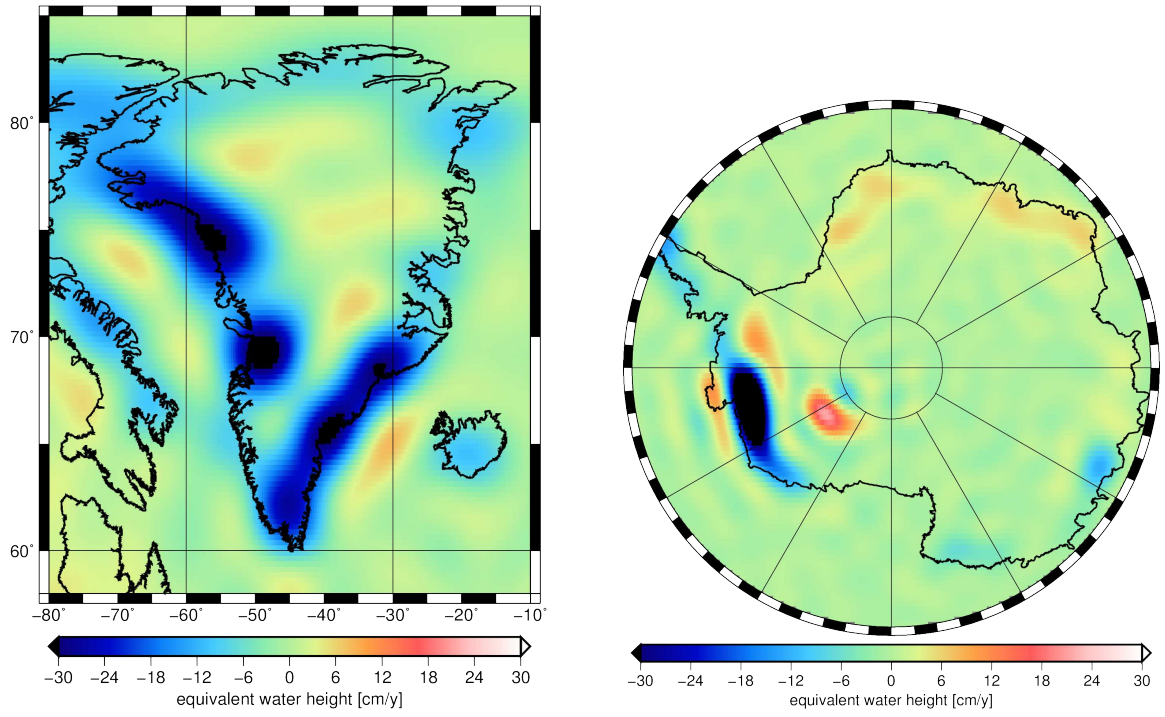

(a) Greenland. (b) Antarctic.

Figure 7.14: Estimated secular temporal variations in terms of equivalent water height per year for selected regions. Min: -57.65 cm/y, Max: 21.89 cm/y.

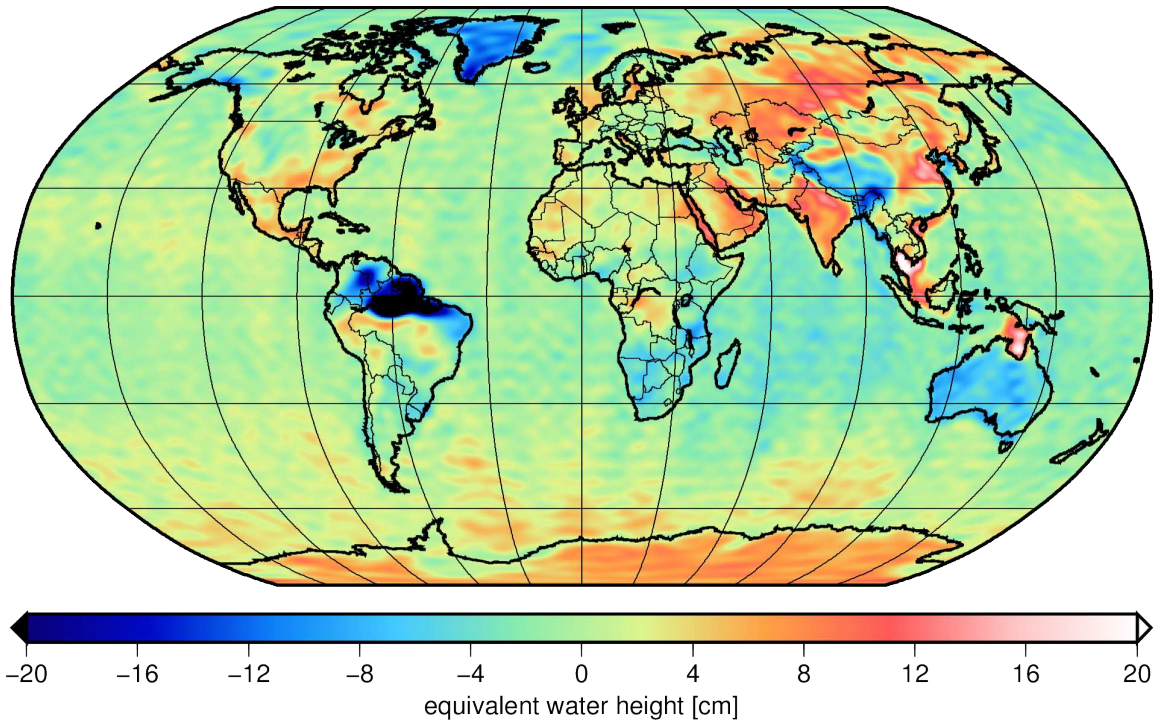

Figure 7.15: Estimated annual temporal variations (cosine coefficiens) in terms of equivalent water height. Min: -62.87 cm, Max: 23.27 cm.

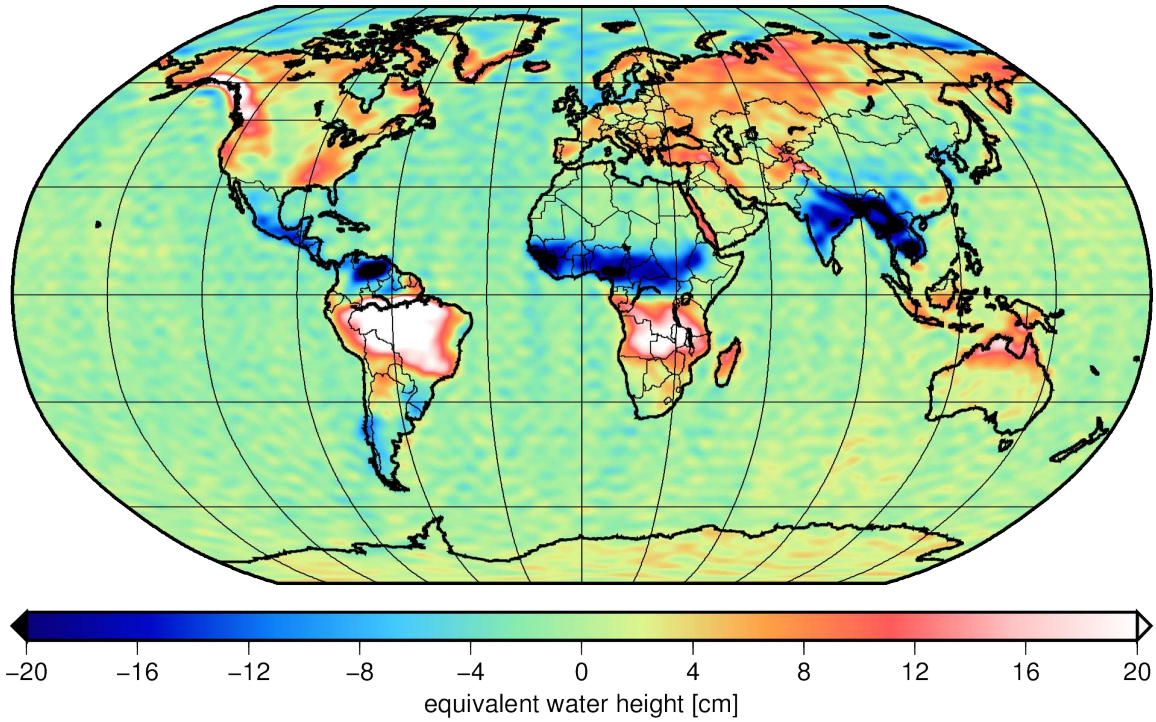

Figure 7.16: Estimated annual temporal variations (sine coefficiens) in terms of equivalent water height. Min: -37.15 cm, Max: 62.11 cm.

8 Summary and Outlook

The prime objective of this work was to develop and implement a flexible algorithm for the combined estimation of Earth's static and time variable gravity field.
In a first step, the general representation of the time variable gravity field is described and adapted to the Gauss-Markoff model on the basis of observation equations. A regularization scheme for short-term temporal variations based on the Kalman-filter approach developed by Kurtenbach, 2011 is formulated. A suitable matrix structure for efficient computation of the combined least squares adjustment is presented. The resulting mathematical model has then been implemented and incorporated into the GRACE processing chain.
The capability of the developed approach was demonstrated on the basis of three computed GRACE-only gravity fields using GRACE-L1B data in the time span of 2004-01 to 2012-12. As is shown in chapter 7 the estimated gravity field models using the combined adjustment approach exhibit a significant improvement over a straightforward static gravity field representation. The overall errors in the mid- to short-wavelength part of the Earth's gravity field are reduced, especially a reduction of errors in the GRACE resonance orders is evident. An impact on the formal errors of the gravity field models can also be observed. The fact that the spherical harmonic coefficients of the GRACE resonance orders can not be determined with the same accuracy as the non-resonance coefficients is reflected in the formal errors of the combined solution. This is not the case when only modeling the static gravity field in the adjustment process.
It can further be seen that the spherical harmonic expansion of the long-term temporal variations should not be truncated before degree and order 100 since time variable signal is still present in higher frequencies.
The implementation of the algorithm was successfully used in the computation of the ITSG-Grace2014s static gravity field model (Mayer-Gürr et al., 2014).
Despite the promising results obtained by the combined adjustment approach, the potential for improvement of various aspects of the method and further investigations still remains.
Since no independent data sets for the investigation of the impact of the incorporation of temporal variations into the adjustment process on the long-wavelength part of the gravity field spectrum are available, a validation using orbit determination should be considered.
The algorithm itself can be improved by implementing adaptive memory determination for each node and a more flexible handling of the memory bound during the computation of the observation equations. This feature will be required when dealing with future satellite missions which may offer a higher sampling rate of the observations or allow a higher spatial resolution of the Earth's gravity field.
To improve the solution, a more thorough modeling of the temporal variations should be considered. Especially geophysical events of discontinuous nature such as earthquakes have to be accounted for to avoid the contamination of continuous gravity field signals. One approach to deal with such phenomena would be a piece wise linear representation within the observation period. Furthermore, different spatial representations of the time variable gravity field, such as space localizing basis functions, could enable a better adaptation to regionally confined mass redistributions.
The application of the developed algorithm to satellite missions which, for example, only provide SST-hl (high-low satellite-to-satellite tracking) observations should also be considered. Even though the SST-hl configuration exhibits lower sensitivity to time variable gravity field signal, possible improvements in static gravity field estimates might occur. This is supported by the fact that the impact of the modeled short- and long-term variations is evident in the short wavelength part of the gravity field where no more time variable signal is observed.

Acronyms

ACC	SuperSTAR Accelerometer
AOD1B	Atmosphere and Ocean De-aliasing Level-1B
CHAMP	Challenging Minisatellite Payload
DLR	Deutsches Zentrum für Luft und Raumfahrt
ESSP	Earth System Science Pathfinder
GFZ	German Research Centre for Geosciences
GOCE	Gravity Field and Steady-State Ocean Circulation Explorer
GPS	Global Positioning System
GRACE	Gravity Recovery And Climate Experiment
JPL	Jet Propulsion Laboratories
KBR	K-Band Ranging System
LEO	Low Earth Orbiter
LRR	Laser Retro Reflector
MTM	Center of Mass Trim Assembly Mechanism
NASA	National Aeronautics and Space Administration
POD	precise orbit determination
SCA	Star Camara Assembly
SLR	Satellite Laser Ranging
SST-hl	high-low satellite-to-satellite tracking
SST-ll	low-low satellite-to-satellite tracking
USO	Ultra Stable Oscillator
UTCSR	University of Texas at Austin, Center for Space Research

List of Figures

List of Tables

List of Algorithms

References

Austen, G. and T. Reubelt (2000). "Räumliche Schwerefeldanalyse aus semi-kontinuierlichen Ephemeriden niedrigfliegender GPS-vermessender Satelliten vom Typ CHAMP, GRACE und GOCE". MA thesis. University of Stuttgart.

Bettadpur, S. (2009). *Recommendation for a-priori Bias & Scale Parameters for Level-1B ACC Data (Version 2)*. Tech. rep. GRACE TN-02.

Bettadpur, S. (2012). *UTCSR Level-2 Processing Standards Document*. Rev 4.0 May 29, 2012, for Level-2 Product Release 0005. URL: `ftp://podaac.jpl.nasa.gov/allData/grace/L2/CSR/RL05/docs/L2-CSR0005_ProcStd_v4.0.pdf`.

Biancale, R. and B. Bode (2006). *Mean Annual and Seasonal Atmospheric Tide Models Based on 3-hourly and 6-hourly ECMWF Surface Pressure Data*. Tech. rep. URL: `http://ebooks.gfz-potsdam.de/pubman/item/escidoc:8692:2/component/escidoc:8691/0601.pdf`.

Bjerhammar, A. (1967). *On the energy integral for satellites*. Tech. rep. Report of the Royal Institute of Technology.

Blackford, L. S., J. Choi, A. Cleary, E. D'Azevedo, J. Demmel, I. Dhillon, J. Dongarra, S. Hammarling, G. Henry, A. Petitet, K. Stanley, D. Walker, and R. C. Whaley (1997). *ScaLAPACK Users' Guide*. Philadelphia, PA: Society for Industrial and Applied Mathematics.

Boxhammer, Christian (2006). "Effiziente numerische Verfahren zur sphärischen harmonischen Analyse von Satellitendaten". PhD thesis. Universität Bonn.

Brockmann, J. M., N. Zehentner, E. Höck, R. Pail, I. Loth, T. Mayer-Gürr, and W.-D. Schuh (2014). "An Independent Geoid with Centimeter Accuracy Purely Based on the GOCE Mission". In: *Geophysical Research Letters*.

Choi, Jaeyoung, Jack J. Dongarra, L. Susan Ostrouchov, Antoine P. Petitet, David W. Walker, and R. Clint Whaley (1994). *The Design and Implementation of the ScaLAPACK LU, QR, and Cholesky Factorization Routines*. Tech. rep. 80. LAPACK Working Note. URL: `http://www.netlib.org/lapack/lawnspdf/lawn80.pdf`.

Desai, S. D. (2002). "Observing the pole tide with satellite altimetry". In: *Journal of Geophysical Research: Oceans* 107 (C11), (7)1–13.

Ditmar, P. and A. A. van Eck van der Sluijs (2004). "A technique for modeling the Earth's gravity field on the basis of satellite accelerations". In: *Journal of Geodesy* 78.1-2, pp. 12–33.

Dobslaw, H. and M. Thomas (2007). "Simulation and observation of global ocean mass anomalies". In: *Journal of Geophysical Research* 112(C05040). DOI: `10.1029/2006JC004035`.

Döll, P., F. Kaspar, and B. Kaspar (2003). "A global hydrological model for deriving water availability indicators: model tuning and validation". In: *Journal of Hydrology* 270, pp. 105–134. DOI: `10.1016/S0022-1694(02)00283-4`.

Dongarra, Jack J., Robert A. van de Geijn, and David W. Walker (1992). *A Look at Scalable Dense Linear Algebra Libraries*. Tech. rep. 43. LAPACK Working Note. URL: `http://www.netlib.org/lapack/lawnspdf/lawn43.pdf`.

Drinkwater, Mark R., R. Haagmans, D. Muzi, A. Popescu, R. Floberghagena, M. Kern, and M. Fehringer (2007). "THE GOCE GRAVITY MISSION: ESA'S FIRST CORE EARTH EXPLORER". In: *Proceedings of the 3rd International GOCE User Workshop, 6-8 November, 2006, Frascati, Italy*. ESA Special Publication, pp. 1–8.

ECMWF Research Department (2013). *IFS Documentation - Chapter III: Dynamics and numerical procedures (40r1)*. Tech. rep.

Flechtner, F., H. Dobslaw, and E. Fagiolini (2014). *AOD1B Product Description Document for Product Release 05*. Tech. rep.

Förste, C., S. Bruinsma, R. Shako, J.-C. Marty, F. Flechtner, O. Abrikosob, C. Dahle, J.-M. Lemoine, H. Neumayer, R. Biancale, F. Barthelmes, R. König, and G. Balmino (2011). *EIGEN-6: A new combined global gravity field model including GOCE data from the collaboration of GFZ-Potsdam and GRGS-Toulouse*. Presented at the 2011 General Assembly of the European Geosciences Union. Vienna, Austria.

Gelderen, M. van and R. Koop (1997). "The use of degree variances in satellite gradiometry". English. In: *Journal of Geodesy* 71.6, pp. 337–343. ISSN: 0949-7714. DOI: 10.1007/s001900050101.

Golub, Gene H. and Charles F. Van Loan (1996). *Matrix Computations*. 3rd ed. Baltimore, MD, USA: Johns Hopkins University Press. ISBN: 0-8018-5414-8.

Heiskanen, W. A. and H. Moritz (1967). *Physical Geodesy*. San Francisco: Freeman.

Higham, Nicholas J. (2002). *Accuracy and Stability of Numerical Algorithms*. 2nd ed. Philadelphia, PA: Society for Industrial and Applied Mathematics.

Ilk, K. H., J. Flury, R. Rummel, P. Schwintzer, W. Bosch, C. Haas, J. Schröter, D. Stammer, W. Zahel, H. Miller, R. Dietrich, P. Huybrechts, H. Schmeling, D. Wolf, H. J. Götze, J. Riegger, A. Bardossy, A. Güntner, and T. Gruber (2005). *Mass transport and mass distribution in the Earth system. Contribution of the new generation of satellite gravity and altimetry missions to geosciences*. Proposal for a German priority research program, 2nd edition. GOCE-Projektbüro TU München, GeoForschungsZentrum Potsdam. URL: http://www.massentransporte.de/fileadmin/Dokumente/programmschrift-Ed2.pdf.

Ilk, K. H. and A. Löcher (2003). "The Use of Energy Balance Relations for Validation of Gravity Field Models and Orbit Determination Results". English. In: *A Window on the Future of Geodesy*. Ed. by Fernando Sansò. Vol. 128. International Association of Geodesy Symposia. Springer Berlin Heidelberg, pp. 494–499. ISBN: 978-3-540-24055-6. DOI: 10.1007/3-540-27432-4_84. URL: http://dx.doi.org/10.1007/3-540-27432-4_84.

Kalman, R. E. (1960). "A New Approach to Linear Filtering and Prediction Problems". In: *Transactions of the ASME - Journal of Basic Engineering* 8, pp. 35–45.

Kaula, W. M. (1966). *Theory of Satellite Geodesy*. Waltham, Massachusetts: Blaisdell Publishing Company.

Koch, Karl-Rudolf (2004). *Parameterschätzung und Hypothesentests in linearen Modellen*. 4th ed. Bonn: Ferd. Dümmlers Verlag. URL: http://www.geod.uni-bonn.de.

Kurtenbach, E. (2011). "Entwicklung eines Kalman-Filters zur Bestimmung kurzzeitiger Variationen des Erdschwerefeldes aus Daten der Satellitenmission GRACE". URN: urn:nbn:de:hbz:5N-25739. PhD thesis. University of Bonn.

Kurtenbach, E., A. Eicker, T. Mayer-Gürr, M. Holschneider, M. Hayn, M. Fuhrmann, and J. Kusche (2012). "Improved daily GRACE gravity field solutions using a Kalman smoother". In: *Journal of Geodynamics* 59-60, pp. 39–48.

Kurtenbach, E., T. Mayer-Gürr, and A. Eicker (2009). "Deriving daily snapshots of the Earth's gravity field from GRACE L1B data using Kalman filtering". In: *Geophysical Research Letters* 36. DOI: 10.1029/2009GL039564.

Kusche, J. (2002). "A Monte-Carlo technique for weight estimation in satellite geodesy". In: *Journal of Geodesy* 76, pp. 641–652.

Mayer-Gürr, T. (2006). "Gravitationsfeldbestimmung aus der Analyse kurzer Bahnbögen am Beispiel der Satellitenmissionen CHAMP und GRACE". URN: urn:nbn:de:hbz:5N-09047. PhD thesis. University of Bonn.

Mayer-Gürr, T. (2013). *Estimation of error covariance functions in satellite gravimetry*. Presented at the 2013 Scientific Assembly of the International Association of Geodesy. Potsdam, Germany.

Mayer-Gürr, T., K. H. Ilk, A. Eicker, and M. Feuchtinger (2005). "ITG-CHAMP01: a CHAMP gravity field model from short kinematic arcs over a one-year observation period". In: *Journal of Geodesy* 78.8, pp. 462–480.

Mayer-Gürr, T., E. Kurtenbach, and A. Eicker (2010a). "Different representations of the time variable gravity field to reduce the aliasing problem in GRACE data analysis." In: *Proceedings of the VII Hotine-Marussi Symposium on Theoretical and Computational Geodesy*.

Mayer-Gürr, T., E. Kurtenbach, and A. Eicker (2010b). *ITG-Grace2010 Gravity Field Model*. URL: http://www.igg.uni-bonn.de/apmg/index.php?id=itg-grace2010.

Mayer-Gürr, T., D. Rieser, E. Höck, J.M. Brockmann, W.-D. Schuh, I. Krasbutter, J. Kusche, A. Maier, S. Krauss, W. Hausleitner, O. Baur O., A. Jäggi, U. Meyer, L. Prange, R. Pail, T. Fecher, and T. Gruber (2012). *The new combined satellite only model GOCO03s*. Presented at the 2012 International Symposium on Gravity, Geoid and Height Systems 2012. Venice, Italy.

Mayer-Gürr, T., N. Zehentner, B. Klinger, and A. Kvas (2014). *ITSG-Grace2014*. Presented at the 2014 GRACE Science Team Meeting. Potsdam, Germany.

McCarthy, D. D. and Petit G., eds. (2004). *IERS Conventions (2003)*. International Earth Rotation and Reference Systems Service (IERS). Frankfurt am Main: Verlag des Bundesamts für Kartographie und Geodäsie. URL: http://www.iers.org/iers/publications/tn/tn32/.

Metzler, B. and R. Pail (2005). "GOCE Data Processing: The Spherical Cap Regularization Approach". English. In: *Studia Geophysica et Geodaetica* 49.4, pp. 441–462. ISSN: 0039-3169. DOI: 10.1007/s11200-005-0021-5. URL: http://dx.doi.org/10.1007/s11200-005-0021-5.

Meyer, Ulrich, Adrian Jäggi, and Gerhard Beutler (2012). "Monthly gravity field solutions based on GRACE observations generated with the Celestial Mechanics Approach". In: *Earth and Planetary Science Letters* 345348, pp. 72–80. ISSN: 0012-821X. DOI: http://dx.doi.org/10.1016/j.epsl.2012.06.026.

Moritz, H. (1980). *Advanced Physical Geodesy*. Karlsruhe: Wichmann.

Niemeier, Wolfgang (2008). *Ausgleichsrechnung - Statistische Auswertemethoden*. 2nd ed. Berlin: de Gruyter.

O'Keefe, J. A. (1957). "An application of Jacobi's integral to the motion of an Earth satellite". In: *The Astronomical Journal* 62.1252, pp. 265–266.

Oppenheim, Alan V., Ronald W. Schafer, and John R. Buck (1999). *Discrete-time signal processing*. 2nd ed. Upper Saddle River, NJ: Prentice-Hall.

Park, J., T.-R. A. Song, J. Tromp E. Okal, S. Stein, G. Roult, E. Clevede, G. Laske, H. Kanamori, P. Davis, J. Berger, C. Braitenberg, M. Van Camp, X. Leiand H. Sun, H. Xu, and S. Rossat (2005). "Earth's free oscillations excited by the 26 December 2004 Sumatra-Andaman earthquake". In: *Science* 308, pp. 1139–1144.

Pavlis, N. K., S. A. Holmes, S. C. Kenyon, and Factor J. K. (2008). *An Earth Gravitational Model to Degree 2160: EGM2008*. Presented at the 2008 General Assembly of the European Geosciences Union. Vienna, Austria.

Reigber, C. (1969). "Zur Bestimmung des Gravitationsfeldes der Erde aus Satellitenbeobachtungen". In: *Deutsche Geodätische Kommision* 137.C.

Savcenko, R. and W. Bosch (2011). *EOT11a - a new tide model from Multi-Mission Altimetry*. Poster, OSTST Meeting San Diego 19-21 October 2011.

Schneider, M. (1968). "A General Method of Orbit Determination". In: *Library Translation*. Vol. 1279. Farnborough, England: Royal Aircraft Establishment, Ministry of Technology.

Schuh, W.-D. (1996). "Tailored numerical solution strategies for the global determination of the earth's gravity field". In: *Mitteilungen der Geodätischen Institute der TU Graz* 81.

Seo, K.-W., C. R. Wilson, J. Chen, and D. E. Waliser (2008). "GRACE's spatial aliasing error". In: *Geophysical Journal International* 172 (1), pp. 41–48.

Standish, E. M. (1998). *JPL Planetary and Lunar Ephemerides, DE405/LE405*. Jet Propulsion Laboratory Interoffice Memorandum, 312.F-98-48.

Tapley, B. D., S. Bettadpur, M. Watkins, and C. Reigber (2004). "The gravity recovery and climate experiment: Mission overview and early results". In: *Geophysical Research Letters* 31, pp. 9607–+.

Tapley, B. D., F. Flechtner, M. Watkins, and S. Bettadpur (2014). *GRACE Mission: Status and Prospects*. Presented at the 2014 GRACE Science Team Meeting. Potsdam, Germany.

U.S. Geological Survey (2014). *PDE (Preliminary Determination of Epicenters)*. URL: `http://earthquake.usgs.gov/data/pde.php`.

Welch, Greg and Gary Bishop (2006). *An Introduction to the Kalman Filter*. Tech. rep. Chapel Hill, NC, USA.

Zehentner, N. and T. Mayer-Gürr (2013). *A new approach for precise orbit determination based on raw GNSS measurements*. Presented at the 2013 General Assembly of the European Geosciences Union.